Planetary and Space Science 95 (2014) 103–119

Contents lists available at ScienceDirect

Planetary and Space Science

journal homepage: www.elsevier.com/locate/pss

Reprint of: Impact craters with ejecta flows and central pits on Mercury

Zhiyong Xiao [a,b,*], Goro Komatsu [c]

[a] Planetary Science Institute, Faculty of Earth Sciences, China University of Geosciences (Wuhan), Wuhan, Hubei 430074, PR China
[b] Lunar and Planetary Laboratory, University of Arizona, Tucson, AZ 85721-0092, USA
[c] International Research School of Planetary Sciences, Università "G. d'Annunzio", Pescara 65127, Italy

ARTICLE INFO

Article history:
Received 10 September 2012
Received in revised form
25 March 2013
Accepted 29 March 2013
Available online 15 July 2013

Keywords:
Mercury
MESSENGER
Impact crater
Ejecta
Central pit

ABSTRACT

Impact craters with ejecta flows and/or central pits have been found on Venus, the Moon, Earth, Mars, and some icy satellites. Using the MESSENGER camera data obtained during the orbital mission, we found craters with ejecta flows and central pits on Mercury. The ejecta flows differ from normal ballistically emplaced ejecta deposits in their long mobilized distances. They all flowed in downslope directions and exhibited a layered morphology. Analog study suggests that the ejecta flows probably have formed by fluidization in the ejecta deposits. Crustal volatiles are not required to form the ejecta flows on Mercury, although they may have helped. The ejecta flows are most likely to be a type of avalanche features in forms of dry granular flows. Central pits in impact craters on Mercury are located on summits of central peaks when viewing in sufficiently high-resolution images, but some of the central pits may occur on crater floors. The central pit craters are all fresh craters located on smooth plains and intercrater plains. The pits are different from the other forms of rimless and irregularly-shaped depressions on Mercury in the size, morphology, and/or occurrence. Crustal volatiles are not required in forming the central pit craters and they may form in a similar way with the central pit craters on the Moon.

1. Introduction

On airless silicate bodies such as the Moon and Mercury, normal continuous ejecta deposits of fresh impact craters form from ballistic emplacement of impact ejecta (e.g., Osinski et al., 2011). Continuous ejecta deposits start from hummocky terrains near crater rims and grade outwardly into radially ridged facies (Shoemaker, 1965). These two facies exhibit no sharp boundaries and have no superposed secondary crater clusters or chains. Without post-impact disturbances of impact melt flows on continuous ejecta deposits (e.g., Bray et al., 2010), these facies have an exponentially decreasing thickness measured radially from crater rims (e.g., McGetchin et al., 1973). Continuous ejecta deposits on the Moon and Mercury usually have a smooth morphology and a limited extent (e.g., Schultz and Singer, 1980; Xiao et al., 2013a), and no ejecta flows occur on continuous ejecta blankets (e.g., Fig. 1).

Crater ejecta that have a fluidized morphology are found on Venus (e.g., Schultz, 1992; Baker et al., 1992), the Moon (Shoemaker et al., 1968; Guest, 1973; Melosh, 1987), Earth (e.g., Osinski, 2004; Kenkmann and Schönian, 2006; Maloof et al., 2010), Mars (e.g., Carr et al., 1977), and some outer Solar System icy satellites such as Europa (Moore et al., 2001), and Ganymede (Passey and Shoemaker, 1982; Boyce et al., 2010). These ejecta have a layered morphology compared with normal ballistically emplaced ejecta deposits. Ejecta flows on Venus were interpreted to form from the entrainment of atmosphere during the ejecta emplacement (e.g., Schultz, 1992). Crustal and/or atmospheric volatiles affect ejecta emplacement on Mars and are possible reasons in forming martian ejecta flows (e.g., Carr et al., 1977; Barlow, 2005; Komatsu et al., 2007). Those on icy satellites were hypothesized to result from the effect of crustal water ice (e.g., Moore et al., 2001). Ejecta avalanches on the Moon were interpreted to be dry granular flows (Melosh, 1987).

Ejecta flows had not been known to exist on Mercury prior to the MErcury Surface, Space ENvironment, GEochemistry, and Ranging (MESSENGER; Solomon et al., 2001) mission. The previous Mariner 10 data covered ~45% of Mercury's surface at an average resolution of ~1 km/pixel. The Mariner 10 data contained a large number of high solar-angle images ($>60^{\circ}$, measured from horizontal) restricting detailed morphological studies for surface features (cf. Strom, 1979). These factors probably prohibited finding ejecta flows on Mercury in Mariner 10 imagery.

Central pits in impact craters have been found on Mars (e.g., Barlow and Bradley, 1990; Robbins and Hynek, 2012), the Moon and Earth (e.g., Milton et al., 1972; Allen, 1975), and on icy moons, especially Ganymede and Callisto (e.g., Passey and Shoemaker, 1982; Croft, 1983; Schenk, 1993; Alzate and Barlow, 2011). The pits

DOI of original article: http://dx.doi.org/10.1016/j.pss.2013.03.015
* Corresponding author is now at: Planetary Science Institute, Faculty of Earth Sciences, China University of Geosciences (Wuhan), Wuhan, Hubei 430074, PR China. Tel.: +86 27 6788 3019.
E-mail addresses: xiaobeary@gmail.com, xiaobear@lpl.arizona.edu (Z. Xiao).

0032-0633/$ - see front matter © 2013 Elsevier Ltd. All rights reserved.
http://dx.doi.org/10.1016/j.pss.2013.07.001

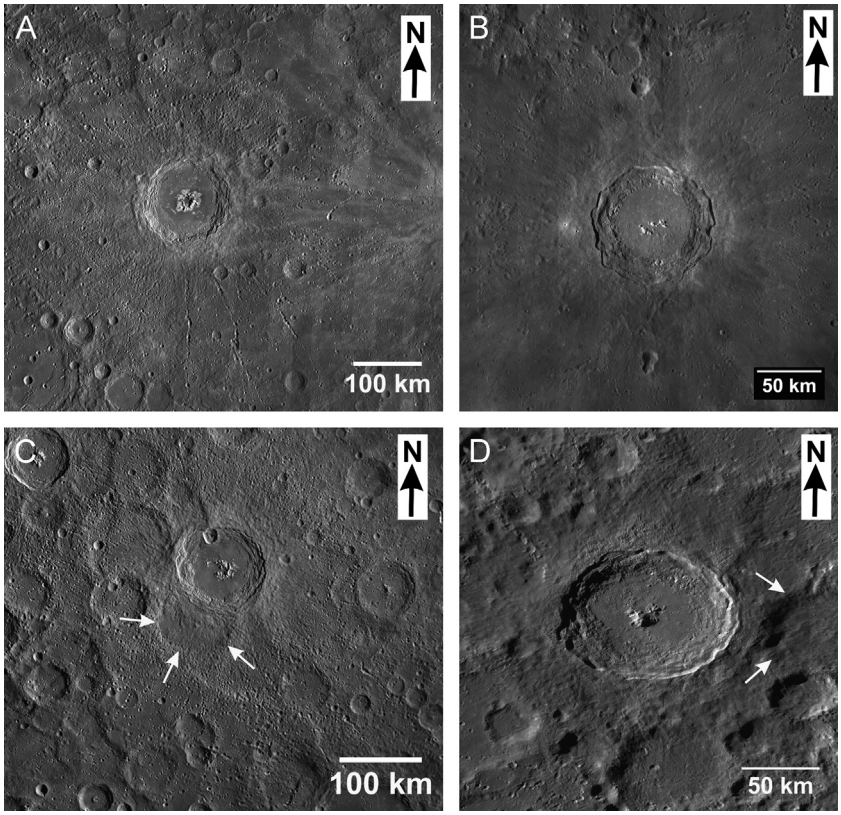

Fig. 1. Ballistically emplaced ejecta deposits of impact craters on the Moon and Mercury. (A) and (C) are the Eminescu (D=130 km; 11 °N, 114 °E) and Amaral (D=109 km; 27 °S, 118 °E) craters on Mercury, respectively. (B) and (D) are the Copernicus (D = 93 km; 10°N, 20°W) and Tycho (D = 85 km; 43°S, 11°W) craters on the Moon, respectively. The base mosaics of (A) and (C) are from the 250 m/pixel global mosaics of Mercury, those of (B) and (D) are from the 100 m/pixel global mosaics of the Moon. The white arrows in (C) and (D) show preexisting topographic lows at the impact sites; impact melt ponded in these areas but no ejecta flows are visible. All the panels are in equirectangular projections.

are either rimless or rimed (Garner and Barlow, 2012; Bray et al., 2012) depressions that are located on summits of central peaks or in centers of crater floors (e.g., Barlow and Bradley, 1990). Previous studies about their origin mostly emphasized the importance of target volatiles during impact processes, which suggested that central pits had formed from either vapor bursts or ice melt drainage (e.g., Barlow and Bradley, 1990; Barlow, 2010; Senft and Stewart, 2011; Bray et al., 2012). Central pits also are interpreted to be caused by impacts into compositionally or rheologically distinct layers at depth (Greeley et al., 1982; Schenk, 1993). The Moon and Mercury generally have been thought to be poor in crustal volatiles (e.g., Lewis, 1972). Central pit craters were not expected to occur on these two bodies (e.g., Elder et al., 2012). Allen (1975) found some craters with central pits on the Moon, but the origin of the pits so far remains unknown due to the assumption of low content of crustal volatiles on the Moon (e.g., Bray et al., 2012). Central pit craters had not been found on Mercury prior to MESSENGER, and the limited coverage and resolution of the Mariner 10 data are possible reasons.

After the three flybys, the MESSENGER spacecraft successfully entered the orbit about Mercury in March 2011. The Mercury Dual Imaging System (MDIS) onboard MESSENGER (Hawkins et al., 2007) has been carrying out systematic global imaging augmented by high-resolution targeted observations. Compared with both the MESSENGER and Mariner 10 flyby data, MDIS orbital images have great improvement in image resolution, coverage, and illumination conditions, thus permitting detailed morphological studies for impact craters.

In this study, we find that several impact craters on Mercury have ejecta flows that are similar in morphology to those on other planetary bodies. Some other impact craters on Mercury have central pits. The ejecta flows and central pits on Mercury provide a complement to similar features on other Solar System bodies, and are therefore useful to understand the formation mechanisms for these features as well as the possible role of volatiles to the impact process.

Here we introduce the morphological and geometrical properties for the ejecta flows and central pits on Mercury. We study their global distribution and compare them with similar morphological features on other planetary bodies. Combining with the geological background and surface conditions on Mercury, we investigate the possible contributing factors in the formation of these features in combination with the geological background and surface conditions on Mercury.

2. Research material

The global monochrome mosaics of Mercury obtained during the MESSENGER orbital mission were used to search for craters with ejecta flows and central pits. The mosaics were composed of MDIS Narrow Angle Camera (NAC) and Wide Angle Camera (WAC) images acquired in the filter centered at 750 nm wavelength. Images in the mosaics were selected and prioritized by resolution, mid to high solar incidence angles, and low emission angles. The mosaics have a resolution of 250 m/pixel and cover over 99.9% of the planet. The detailed information about the mosaics is found at http://messenger.jhuapl.edu/the_mission/mosaics.html. We also made regional mosaics for each of the observed ejecta flows and central pits to measure their geometric properties. The mosaics were in sinusoidal projections and were centered on the centers of the parent craters to preserve accurate areal

information. The USGS's Integrated Software for Imagers and Spectrometers (http://isis.astrogeology.usgs.gov/) was employed in making the mosaics.

Mercury Laser Altimeter data (MLA; Cavanaugh et al., 2007; Zuber et al., 2012) and MDIS stereo mosaics are presently not available in the public domain for the observed ejecta flows and central pit craters. To provide a first order topographic analysis, we applied shadow-height measurements for the reliefs of the ejecta flows and the depths of the central pits. We also compared the observed ejecta flows on Mercury with normal ballistically-emplaced ejecta deposits on both the Moon and Mercury to better show their mobilized morphology. The global mosaics of the Moon obtained by the Lunar Reconnaissance Orbiter Camera Wide Angle Camera (LROC WAC; Robinson et al., 2010) were used (100 m/pixel). The detailed description of the LROC WAC mosaics is at http://wms.lroc.asu.edu/lroc/global_product/100_mpp_global_bw.

3. Impact craters with ejecta flows and central pits on Mercury

3.1. Craters with ejecta flows

Impact craters with ejecta flows are rare on Mercury. Seven candidate examples with a diameter range of ~35–90 km are found at the time of this writing (Table 1; Figs. 2 and 3). The ejecta flows are more extensive than normal ballistically emplaced ejecta deposits on Mercury (Fig. 1). The seven examples can be roughly classified into two morphological groups (Figs. 2 and 3), depending on the presence or absence of a pronounced digitate toe structure along the ejecta margins.

The three ejecta flows shown in Fig. 2 have sinuous margins and appear as plateaus abutting the underlying terrain. The ejecta extended as far as ~35 km from the rims of their parent craters, ~0.4–0.6 crater radii of the parent craters, exhibiting a fluidized morphology. The three ejecta flows have several common morphological characteristics, which include:

(1) The surfaces of the ejecta flows appear to be relatively rough compared with normal ballistically emplaced ejecta deposits (e.g., Fig. 1). Small undulations occur on the ejecta flows and the flow margins are steep in appearance.
(2) Most of the ejecta flows seem to have a constant thickness along the flow direction and no obvious elevated escarpments (i.e., ramparts) are visible at the majority of the flow margins. At limited sections of the flow margins, raised rims and/or thickened deposits (blue arrows in Fig. 2A and B) possibly exist, but these observations are near the limits of image resolution (100–225 m/pixel).
(3) No radial striations or secondary craters (secondaries) are visible on the ejecta deposits as seen at the present image resolutions. Small curves, which may represent segregation lines (Shreve, 1968), occur at some places on the flows and appear convex in the flow directions (e.g., dashed arrow in Fig. 2B).
(4) The parent craters of the ejecta flows are in different degradation states, and they all occur along the rims of pre-existing older craters. Using the Lunar and Planetary Laboratory crater classification criteria (Class 1 is the freshest and Class 6 is the most degraded; e.g., Wood and Anderson, 1978), the parent craters are morphological Class 1 (Fig. 2A) to Class 3 (Fig. 2C) craters.
(5) The ejecta flows usually do not extend completely around their parent craters. They were preferentially emplaced downslope and are deposited in the floors of the underlying craters (yellow arrows in Fig. 2). Notably, rims of degraded older craters are visible but partially overlain by the ejecta flow shown in Fig. 2A (white arrows and dashed circles). The ejecta flows are sometimes constrained by local topographic undulations suggesting their ground hugging nature (cf. Komatsu et al., 2007; Fig. 2B).

Moreover, obvious bright haloed hollows (Blewett et al., 2011, 2013) occur in some of the parent craters (e.g., Fig. 2C) indicating the pre-impact surfaces might have been relatively rich in volatiles compared to the average of the planet (Blewett et al., 2013; Xiao et al., 2013b).

The other four ejecta flows on Mercury do not have obvious sinuous margins but show semicircular, tapered or tongue-like morphologies (Fig. 3). Individual ejecta flows appear to have a constant thickness and no obvious terminal ramparts are visible. Similar to the ejecta flows shown in Fig. 2, the parent craters of the four ejecta flows in Fig. 3 are morphological Class 1–3 craters and they are all located along rims of older craters. The ejecta preferentially moved downslope and rested in the floors of the underlying craters. The flows are ~25–45 km long, ~0.5–0.6 radii of their parent craters. No radial striations (grooves or ridges), surrounding levees, secondaries, or multi-layers are visible on the flows seen at the present image resolutions (~200–400 m/pixel). Sculpture curves on the ejecta appear convex in the flow directions (e.g., Fig. 3A).

The geometry of fluidized ejecta deposits is a key to understanding their mode of emplacement (e.g., Hack, 1960; Ritter et al., 2006). We collected some geometric parameters for the ejecta flows on Mercury, including the rim to rim diameter of the parent crater (D), the longest distances from crater rims to edges of the ejecta (L), the perimeters (P), surface areas (A), and heights (h) at the flow edges. L is called the ejecta extent or runout distance (e.g., Barlow, 2005). We performed more than 5 measurements for each of these parameters and used the average values. The standard deviations of the multi-measurements were used as the errors to

Table 1
Geometric parameters for the seven craters with ejecta flows on Mercury (Figs. 2 and 3).

ID	Lat	Lon	D (km)	L (km)	P (km)	A (km^2)	h (m)[a]	EM	Γ
2A	27	−51	88 ± 1.1	35 ± 0.7	488 ± 7.2	8501 ± 192	~390–470	0.80 ± 0.01	1.49 ± 0.2
2B	45	−71	60 ± 0.8	34.8 ± 0.5	205 ± 6.1	2702 ± 70	–	1.16 ± 0.02	–
2C	14	−63	77 ± 0.6	35.6 ± 0.6	191.6 ± 5.9	2668 ± 83	~450–520	0.93 ± 0.02	–
3A	48	−139	37.5 ± 1.5	24.2 ± 0.5	103 ± 1.5	631 ± 13.6	~320–430	1.29 ± 0.27	–
3B	−20	27	39.5 ± 2.2	24.3 ± 0.2	108 ± 3.1	564 ± 27.4	–	1.23 ± 0.18	–
3C	−56	18	83.7 ± 3.7	44.8 ± 0.6	206 ± 5.2	2204 ± 3.8	~590	1.15 ± 0.32	–
3D	−4	−59	40 ± 1.1	22.9 ± 0.2	154 ± 2.4	1159 ± 13.9	~350–550	1.15 ± 0.31	–

[a] From top to bottom, the base images used for the five height (h) measurements are: EW0213373693G (207 m/pixel; θ=73°); EW0213634699G (118 m/pixel; θ=68°), EW0212285623G (243 m/pixel; θ=71°), EN0220746637M (388 m/pixel; θ=67°), and EW0223659303G (273 m/pixel; θ=58°). θ is the sun incidence angle measured from horizontal. The illumination conditions in EW0223874385G (Fig. 2B; 118 m/pixel; θ=76°) and EN0219983922M (Fig. 3C; 188 m/pixel; θ=70°) are not suitable to measure the height values for the flow fronts. For each example, h shows a wide range because the selected sites are at different locations along the flow margins.

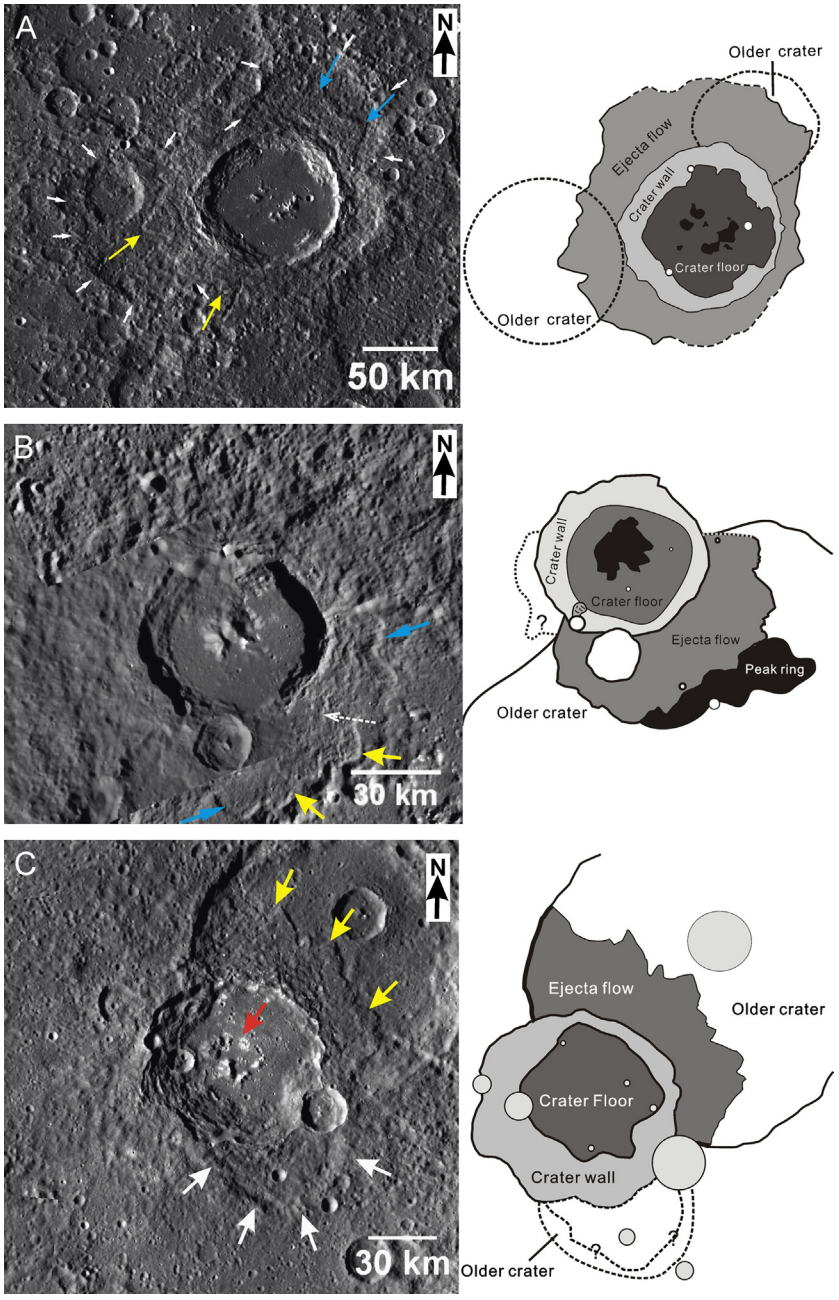

Fig. 2. Candidate ejecta flows on Mercury that have sinuous edges. (A) An ejecta flow occurs around an unnamed crater (D=88 km; 27 °N, 51 °W) in heavily cratered terrain. This crater is a morphological Class 1 or 2 crater. The white arrows show rims of the underlying older craters. The blue arrows point to potential distal escarpments. The mosaic (214 m/pixel; sinusoidal projection) was made from MDIS frames EW0213373662G, EW0213373693G, EW0213417143G, EW0213417154G, EW0213417177G, EW0213417188G, and EW0213460629G. (B) An ejecta flow occurs along the southern rim of unnamed crater (D=60 km; 45 °N, 71 °W). This crater is a morphological Class 1 or 2 crater. The blue arrows point to potential terminal ramparts. The dashed arrow points to a sculpture curve on the deposit. The base image is from the global monochrome mosaics of Mercury (250 m/pixel; equirectangular projection). (C) A morphological Class 2 or 3 crater (D=77 km; 14 °N, 63 °W) has ejecta flows at its northeastern crater rim. Hollows occur in the center of the crater (red arrow). The base image is from EW0213547734G, EW0213547787G, EW0213591178G, EW0213591190G, EW0213591231G, EW0213591243G, EW0213634645G, EW0213634699G, and EW0213634710G (sinusoidal projection; 221 m/pixel). In all the figures, the yellow arrows point to aprons along the edges of the ejecta flows. The right panels show the schematic diagrams for the ejecta flows. (For interpretation of the references to color in this figure legend, the reader is referred to the web version of this article.)

assess the reliability of our measurements. The flow-front heights (h) were estimated from shadow-height measurements. Calculated from $h=l\times\tan(\theta)$ (l is the length of shadow and θ is the solar angle measured from horizontal), h served as a proximal value because the edges of the ejecta flows were not vertical and the slopes of underlying terrain were not considered. Table 1 shows that the seven ejecta flows have a comparable thickness at the rims varying from ~300 to 600 m. The height value has a range because we selected different locations along the flow margins for the measurement.

We calculated the ejecta mobility (EM) and lobateness (Γ) for the ejecta flows. EM provides information about the fluidity of the ejecta flows at the time of emplacement. EM is the ratio between the ejecta extent (L) and the crater rim–rim radius (R; Eq. (1))

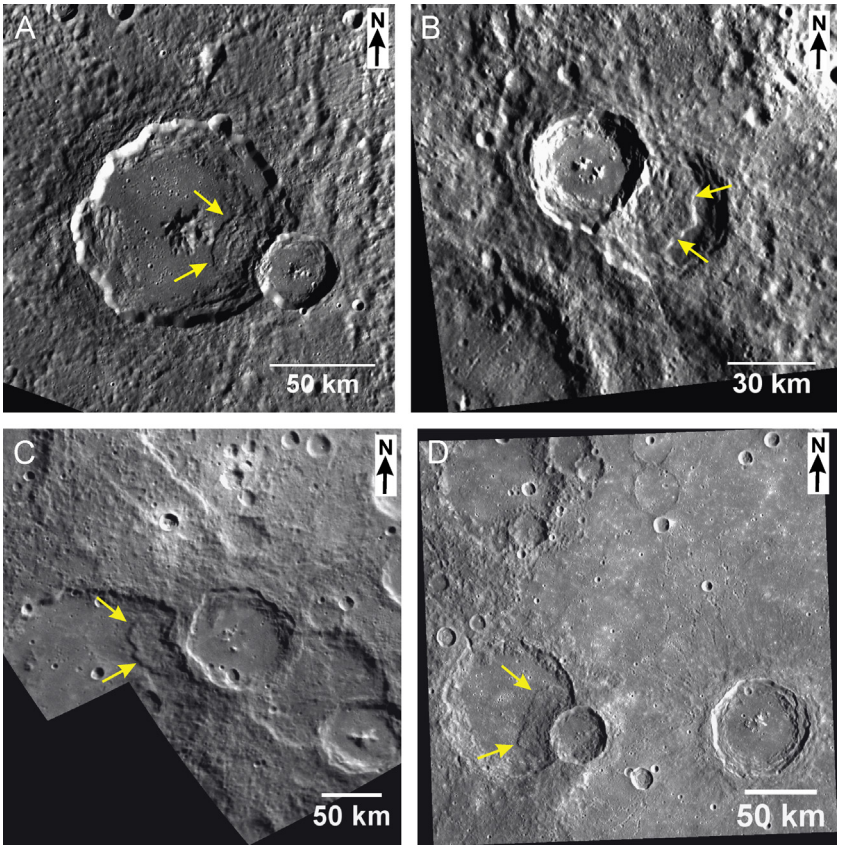

Fig. 3. Ejecta flows on Mercury that have semicircular edges. The base images for panels (A) to (D) are EW0212285623G (243 m/pixel), EN0219983922M (188 m/pixel), EN0220658605M (388 m/pixel) and EW0223659303G (273 m/pixel), respectively. The yellow arrows point to the rims of the ejecta flows. The images are in sinusoidal projections. (For interpretation of the references to color in this figure legend, the reader is referred to the web version of this article.)

(Mouginis-Mark, 1979).

$$EM = \frac{L}{R} \quad (1)$$

The errors of *EM* were calculated from those of *L* and *D* (Table 1). The results (Table 1) show that smaller craters generally have larger *EM* ratios, e.g., the ejecta flow shown in Fig. 2A versus the one shown in Fig. 3A (Table 1). Also interestingly, the ejecta flows that terminate with digitate toe structures (Fig. 2) generally have smaller *EM* ratios compared with those having semicircular margins (Fig. 3).

Lobateness (Γ) is a measure of ejecta sinuosity (Kargel, 1989; Barlow, 1994) and it is calculated from the ejecta perimeter (*P*) and surface area (*A*). Γ evaluates the viscosity difference between the ejecta flow and the underlying terrain (Snyder and Tait, 1998). The definition of Γ is:

$$\Gamma = \frac{P}{(4\pi A)^{0.5}} \quad (2)$$

The error of Γ is calculated from those of *P* and *A* (Table 1). $\Gamma = 1$ means the ejecta are symmetrically circular in shape; larger Γ means the ejecta are more irregular in shape. Most of the ejecta flows only occur at some parts of the crater rims, thus their lobateness is not obtainable. We can roughly estimate the lobateness only for the ejecta flow shown in Fig. 2A (in fact, some sections of the ejecta flow are inferred as indicated by the dashed lines in the schematic diagram).

3.2. Craters with central pits

We found 27 impact craters on Mercury that have irregularly-shaped and sometimes circular or elongated depressions in the crater centers (Table 2). When viewing in images with sufficiently high resolution, the pits all occur on summits of central peaks (Fig. 4). These depressions are summit pits following the definition for similar features on Mars (e.g., Barlow, 2010). Some other central pits on Mercury appear to occur on crater floors and have surrounding uplift massifs (Fig. 5). These pits could be rimed floor pits which are similar to those found on Ganymede (Bray et al., 2012) and Mars (Garner and Barlow, 2012), or they could represent summit pits that have penetrated through central peaks. Future higher-resolution images will help to reveal the precise locations for the pits and to determine whether the pits are rimless or have low rims. In planar morphology, the circular and elongated pits somewhat resemble cone craters (e.g., Fig. 4B), but no debris deposits or flow material are visible around the central pits in the present image resolution (100–250 m/pixel).

All the central pit craters on Mercury are morphological Class 1 craters and have a diameter range of ~16–33 km (Table 2). Some of these craters have distinctive impact rays (e.g., Fig. 4B) indicating the craters and thus the pits are very young features. The central pit craters are located on plains material (Table 2), including smooth plains (SP; 63%) and intercrater plains (IP; 37%). For example, Fig. 4A shows a summit-pit crater ($D = 26$ km; 67.1 °N, 61.6 °E) in the northern volcanic plains (Head et al., 2011) and Fig. 5A shows a central pit crater ($D = 14$ km; 21.0 °N, 166.5 °W) in the Caloris exterior plains (Strom et al., 2008; Denevi

Table 2
Geometric parameters for the central-pit craters on Mercury.

Lat (°N)	Lon (°E)	A_c	A_p	d (m)[a]	Image-ID	Background[b]	D_c	D_p	D_p/D_c
20.0	63.6	227.1	2.7	280	EN0219350124M	IP	17.01	1.86	0.11
67.1	61.6	508.6	4.6	380	EW0219648898G	NP	25.45	2.41	0.09
57.7	33.0	333.2	5.7	300	EW0219988602G	NP	20.60	2.68	0.13
57.5	32.1	224.2	4.3	360	EW0219988602G	NP	16.90	2.34	0.14
21.0	−166.5	150.3	6.2	230	EN0212675835M	CEP	13.83	2.82	0.20
0.8	−175.5	221.5	3.0	300	EN0212935377M	CEP	16.79	1.95	0.12
0.4	−177.6	664.3	5.6	460	EN0212978685M	CEP	29.08	2.66	0.09
−77.1	−160.9	365.5	3.1	270	EN0215423321M	IP	21.57	2.00	0.09
−21.8	153.3	552.6	9.1	–	EN0215678334M	IP	26.52	3.41	0.13
−22.7	152.5	553.1	5.7	–	EN0215678334M	IP	26.54	2.69	0.10
6.3	70.8	216.0	2.8	340	EN0219051977M	SP	16.58	1.90	0.11
13.3	74.3	326.9	5.3	420	EN0219094814M	SP	20.40	2.60	0.13
17.0	26.1	850.2	16.2	490	EN0219944877M	IP	32.90	4.54	0.14
30.5	1.5	231.0	3.7	230	EN0220675584M	IP	17.15	2.16	0.13
26.9	118.7	228.0	1.7	–	EW0216068263G	SP	17.04	1.46	0.09
39.7	25.6	213.0	2.9	330	EW0220030595G	IP	16.47	1.91	0.12
−23.3	−54.4	302.1	2.5	260	EN0213418350M	IP	19.61	1.77	0.09
69.8	−90.9	334.2	4.8	270	EW0211764553G	NP	20.63	2.48	0.12
68.7	−93.2	211.4	5.5	170	EW0211764553G	NP	16.41	2.66	0.16
44.6	126.1	783.0	7.8	420	EW0216154818G	CEP	31.58	3.15	0.10
54.3	55.3	489.2	9.0	330	EW0219648668G	CEP	24.96	3.38	0.14
57.8	38.8	252.4	4.3	270	EW0219946120G	NP	17.93	2.34	0.13
51.6	31.2	329.7	7.2	330	EW0219988455G	NP	20.49	3.02	0.15
38.7	140.6	748.9	17.2	–	EW0220763820G	CEP	30.88	4.68	0.15
23.8	143.4	465.6	5.1	250	EW0220764060G	CEP	24.35	2.55	0.10
44.7	126.1	628.1	9.9	470	EW0220979754G	CEP	28.28	3.54	0.13
36.6	−83.9	752.3	6.4	530	EW0211546523G	IP	30.95	2.86	0.09

[a] The depths of the central pits are estimated from shadow-height measurements as the minimum values. Some base images do not have suitable illumination conditions for the measurements thus the depth values are not obtainable.

[b] Background terrain of the observed central-pit craters on Mercury. Classification criteria are referred from Denevi et al. (2009, 2012). IP denotes intercrater plains, NP denotes northern plains (Head et al., 2011), and CEP denotes Caloris exterior plains (Strom et al., 2008; Murchie et al., 2008).

et al., 2009). Statistically, most craters on Mercury within this diameter range do not have a central pit, and similar-sized craters with similar degradation states in a same region may or may not have central pits. For example, in Fig. 4C, the crater pointed by the white closed arrow (D=29 km; 44.7 °N, 126.1 °E) has a pit on the central peak, whereas similar-sized craters nearby (white open arrows) do not have central pits.

We measured the surface areas for both the central pits (A_p) and their host craters (A_c). D_p and D_c are the equivalent diameter values calculated from A_p and A_c respectively. The plots of A_p versus A_c and D_p versus D_c are shown in Fig. 6. A_p/A_c varies from ~0.01 to 0.04. D_p/D_c is ~0.1–0.2 with a median value of 0.12. The coefficients of determination in both Fig. 6A and B are small (0.49) suggesting that same-sized craters can have different sizes of central pits and the difference can be as large as ~2 times. Barlow (2010) and Bray et al. (2012) noticed that central pit craters on Mars and Ganymede have a proportional size relationship of D_p/D_c. A probable reason is that their statistics were based on a larger number of sampled craters, i.e., the number of their sampled craters was hundreds (e.g., Barlow, 2010) but only 27 central pit craters have been found on Mercury.

Assuming that the inner slopes of the central pits were vertical in slopes and their shadow length was less that the width of the pit floor, we used shadow-height measurement to estimate the minimum depths for the central pits (d). Table 2 shows the results. The depth (d) and diameter (D_p) of the central pits and the size of their parent craters (D_c) do not have a strictly proportional size relationship, although larger craters generally have larger and deeper central pits (Fig. 6). Central pits of same-sized craters can have different depths by a factor of as large as ~3 (Fig. 6C). Pit-depth also greatly varies among central pits that have a same diameter (D_p; Fig. 6D).

3.3. Global distributions of craters with ejecta flows and central pits

The global distributions of craters with ejecta flows and central pits on Mercury are shown in Fig. 7. Most of the craters (>96%) are located at latitudes north of 30 °S. A probable reason is that MDIS acquires higher resolution images in the northern hemisphere due to the highly elliptical orbit of MESSENGER (Hawkins et al., 2007). The seven craters with ejecta flows show a concentration (4 of 7) in the longitude ranges of ~260°–320 °E, but the statistics are not robust due to the small number of samples. The central pit craters appear to occur at almost all longitudes on Mercury, including within the northern volcanic plains and the Caloris interior plains (Table 2).

This inventory is not complete because the base mosaics do not cover the whole planet (>99.9%). Some portions of the mosaics have high solar incidence angles that are not favorable to searching for such features. In addition, some small craters (D < ~16 km) may have ejecta flows and central pits but they have not yet been covered by high-resolution images. As high-resolution images continue being returned from the MESSENGER mission, more craters with ejecta flows and central pits may be identified in the future.

4. Discussion

4.1. Comparison between the ejecta flows on Mercury and similar features on other planetary bodies, and implications for their formation mechanisms

Ejecta flows have been found on various planetary bodies. For those on Mars, different morphological names, such as rampart

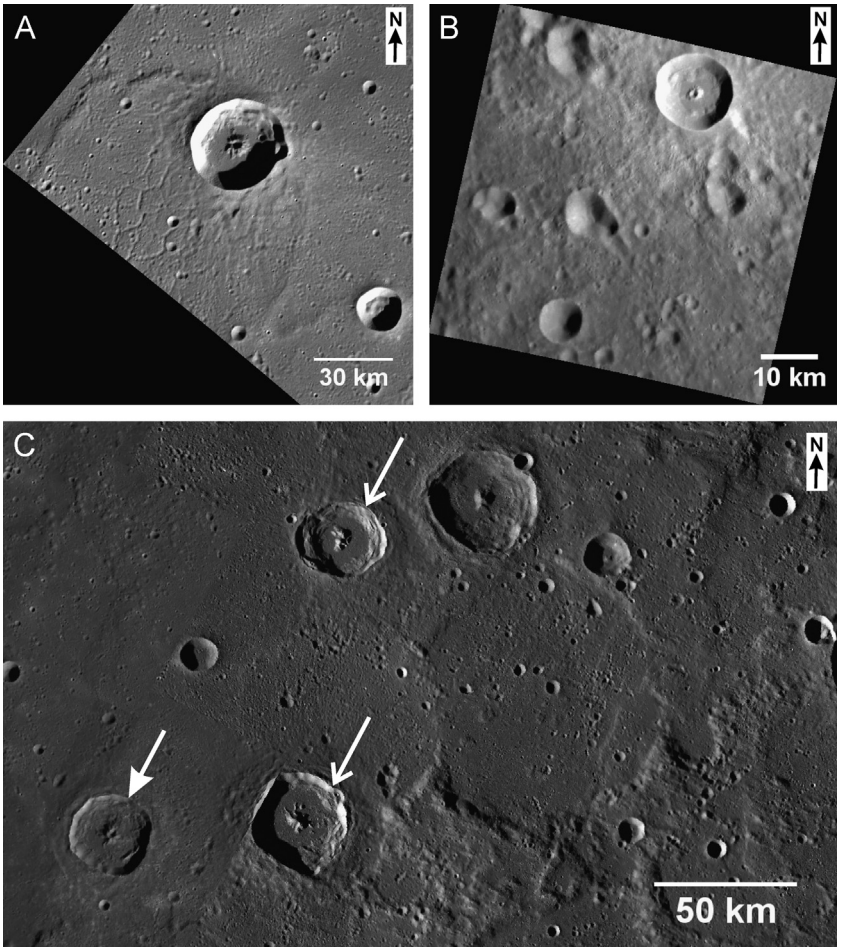

Fig. 4. Examples of central-pit craters on Mercury. (A) and (B) are central-pit craters on the northern plains and Caloris exterior plains, respectively. (C) Similar-sized craters in a same region can have (white closed arrow) or not have (white open arrows) central pits. The base image of (A) is EW0219648898G (133 m/pixel) and (B) is from EN0219350124M (114 m/pixel) and both of them are in sinusoidal projections. (C) is from the MDIS global monochrome mosaics (250 m/pixel; equirectangular projection).

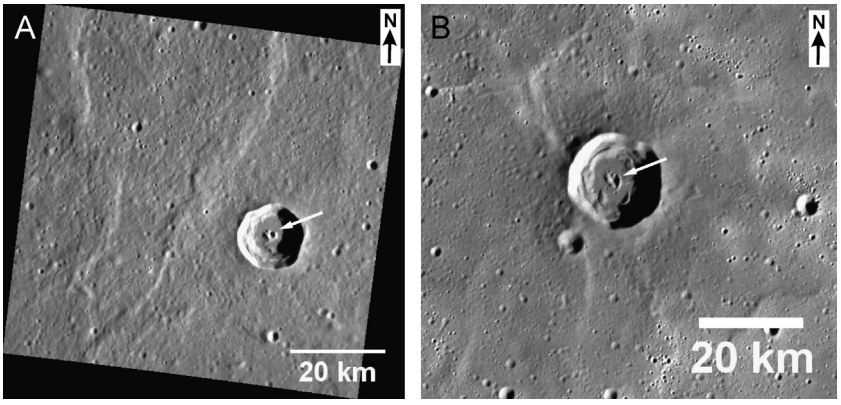

Fig. 5. Some central pits in impact craters may occur on crater floors. (A) A fresh crater in smooth plains has a central pit (white arrow). The pit is possibly located on the crater floor. The base image is MDIS EW0223659303G (273 m/pixel; sinusoidal projection). (B) A fresh crater on the northern plains has a central pit in the crater center (white arrow). The base image is from MDIS EW0219946120G and is in sinusoidal projection (167 m/pixel).

ejecta, layered ejecta, lobe ejecta, pedestal ejecta, pancake ejecta, etc., have been used. Barlow et al. (2000) standardized the nomenclature system for the ejecta flows on Mars using single-, double-, and multi-layered ejecta (collectively termed layered ejecta structures) judging by the number of visible layers on the ejecta. This nomenclature system has been applied for similar layered ejecta deposits on other planetary bodies (e.g., Boyce et al., 2010). The seven ejecta flows on Mercury appear to be a single layer abutting background terrain (Figs. 2 and 3). In this regard, they could be classified as single layered ejecta (SLE) deposits (cf. Barlow et al., 2000), although they are not necessarily identical to those on Mars in origin.

After the first discovery of ejecta flows on Mars over 30 years ago (e.g., Carr et al., 1977), a common consensus has been reached that ejecta flows on planetary surfaces were fluidized during emplacement (e.g., Carr et al., 1977; Boyce et al., 2010). However, their possible modes of emplacement is far from been settled, especially when comparing similar features on different planetary

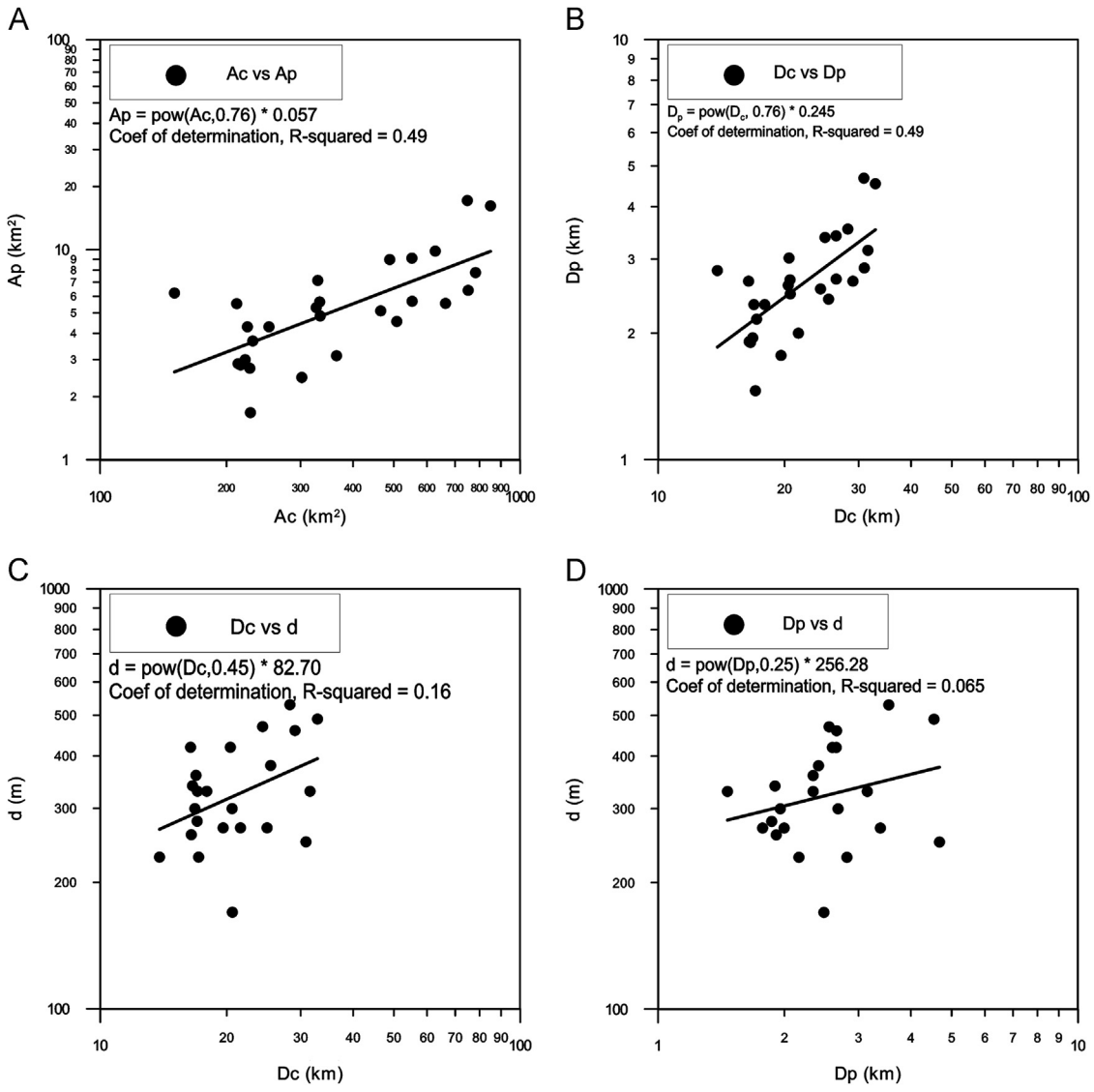

Fig. 6. Size ratio of central pits and their host craters on Mercury. A_c is the surface area of the central-pit crater; A_p is the surface area of the central pits; D_c is the crater rim to rim diameter; D_p is the diameter of the central pits, d is the depth of the central pits. The size relationships are based on the measured results shown in Table 2. The figures are displayed in log–log plot fitted by power law functions and the parameters are listed in the figures.

bodes. Fundamentally, the morphology of ejecta flows is likely affected by a number of factors including surface gravity, density of atmosphere, surface roughness, slope of overlying terrain, fluidity (rheology) of the ejecta, angle and velocity of the ejected material (e.g., Mouginis-Mark, 1978; Kargel, 1989; Barlow, 2005; Barnouin-Jha et al., 2005; Komatsu et al., 2007; Boyce et al., 2010). The ejecta flows on Mercury are not affected by atmosphere so this factor can be ignored.

In this section, we (1) evaluate the fluidity of the ejecta flows on Mercury by comparing them with layered ejecta structures, particularly SLE, on other planetary bodies; (2) investigate the controlling factors in forming the mercurian ejecta flows; (3) compare the ejecta flows on Mercury with similar morphological features on other planetary bodies to investigate their possible identities.

4.1.1. *Fluidity of the ejecta flows on Mercury*

The fluidity of ejecta flows is quantitatively shown in their ejecta mobility (*EM*) and lobateness (Γ) because higher fluidity increases *EM* ratios and larger fluidity difference between the ejecta and ambient terrain increases Γ (e.g., Barlow, 2006; Snyder and Tait, 1998). On Mars, the fluidity of ejecta is considered to be controlled by the volatile content in the ejecta (e.g., Stewart et al., 2001) and/or the degree of interaction of the ejecta curtain with the atmosphere (e.g., Schultz, 1992).

Table 3 shows a comparison for the *EM* and Γ of the seven ejecta flows on Mercury and those of SLE deposits on other planetary bodies. The lobateness (Γ) of the ejecta flows on Mercury is statistically meaningless because only one example (Fig. 2A) has a roughly estimated Γ value. The average *EM* ratio of the ejecta flows on Mercury is slightly larger than that of the icy satellites, but it is smaller than that of both the Mars and Earth (i.e., Lonar crater; Boyce et al., 2010). The ejecta flows on Mercury have a comparable *EM* ratio within error bars with that of the Tsiolkovsky ejecta flow on the Moon. Barlow (2005) and Boyce et al. (2010) found that the *EM* of SLE deposits on a same planetary body is greatly variable with crater diameters and locations, e.g., the *EM* ratio of SLE deposits on Mars is between 0.2 and 6.6 (Barlow, 2005). We also identified the same characteristics for the ejecta flows on Mercury as the *EM* ratio varies

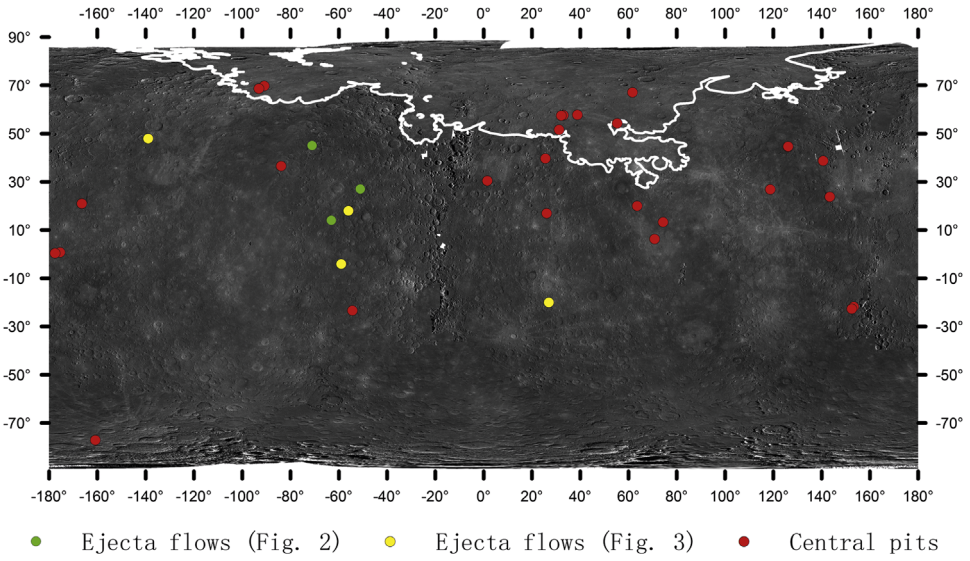

Fig. 7. Distribution of craters with central pits (red dots) and ejecta flows on Mercury (those with sinuous edges are indicated by green dots and those with semicircular edges are indicated by yellow dots). The inventory of the ejecta flows is listed in Table 1 and that of the central-pit craters is in Table 2. The white outline shows the boundaries of the northern plains (Head et al., 2011). The base image is the MDIS global monochrome mosaics in equirectangular projection (250 m/pixel). (For interpretation of the references to color in this figure legend, the reader is referred to the web version of this article.)

Table 3
Average ejecta mobility ratio (*EM*) and lobateness (Γ) for the ejecta flows on Mercury, the Moon, the Earth, Mars, Ganymede, and Europa.

Planetary body and ejecta flows	Average *EM*	Average Γ
Mercury ejecta flows (Table 1)	1.10 ± 0.16	1.49 ± 0.2[a]
Mars single layered ejecta (Barlow, 2005)	1.53	1.10
Ganymede single layered ejecta (Boyce et al., 2010)	1	1.12
Europa pedestal ejecta (Boyce et al., 2010)	0.81	1.1
Earth (Lonar; Boyce et al., 2010)	2.34	1.1
Lunar Tsiolkovsky ejecta flow (Fig. 9D)	1.22	–

[a] Six of the seven ejecta flows on Mercury are only visible around limited parts of the crater rims, thus their lobateness is not obtainable (Table 1). This value is for the ejecta flow shown in Fig. 2A.

from ~0.8 to 1.3 (Table 1). In general, the mobility of the ejecta flows on Mercury is comparable to that of similar features on other planetary bodies indicating the ejecta flows were fluidized during emplacement.

4.1.2. Possible factors affecting the formation of the ejecta flows on Mercury

Based on the common morphological characteristics of the ejecta flows on Mercury, we investigated possible factors affecting their formation processes.

Slope of underlying terrain. The seven craters having ejecta flows on Mercury are located on pre-existing slopes and the ejecta all flowed to the floors of the underlying craters. This observation indicates that pre-existing slopes at impact sites is a necessary element in forming the ejecta flows. On the other hand, however, the majority of impact craters on the Moon and Mercury that formed on slopes do not have ejecta flows (Fig. 8) suggesting that slope alone cannot form the ejecta flows.

High surface temperature. The highest surface temperature on Mercury is ~430 °C. High temperatures tend to lower the viscosity of material and increase its mobility. Moore et al. (1998) argued that thermal creep might be important in forming pedestal ejecta (single layered) on both Europa and Ganymede; i.e., instead of being primary ejecta morphology, these layered ejecta deposits formed from gravity-driven creep. On Mercury, the ejecta flows do not preferentially occur on equator facing slopes where insolation is enhanced (Figs. 2 and 3), and most impact craters formed on pre-existing slopes do not have such ejecta flows (Fig. 8). These observations indicate that the high surface temperature on Mercury is not a controlling factor in forming the ejecta flows.

Large impact velocity. Projectiles striking Mercury have a larger median impact velocity (42.5 km/s) than those on the Moon (19.4 km/s; Le Feuvre and Wieczorek, 2008). Larger impact velocities produce larger volumes of impact melt (Cintala, 1992) and greater comminution in target materials, which may promote the fluidization of ejecta flows (see the next section).

Volatiles. Diverse ejecta morphologies can be explained by impacts into materials with varying proportions of volatiles (Stewart et al., 2001; Baratoux et al., 2002). Volatiles in target materials can affect the final shape of ejecta deposits in the following ways: (1) impacts in volatile-rich target materials form more melting and vaporization (O'Keefe et al., 2001). A higher volatile content in the ejecta generally means less friction between particles and as a result longer transport distances and more aprons along the edges (Wohletz and Sheridan, 1983). (2) During the impact process, expansion of volatiles pushes more displaced material from the excavation cavity, promoting ejecta to flow (Alvarez et al., 1995).

A surprising finding about Mercury revealed by the MESSENGER mission is that the abundances of surface volatiles are higher than previously predicted by high-temperature formation scenarios of Mercury (cf. Peplowski et al., 2011; Nittler et al., 2011). For example, the sulfur content in some locations on Mercury is estimated to be as high as ~4 wt%. Surface units that are possibly related to crustal volatiles are also widely observed on Mercury, such as the bright haloed hollows (Blewett et al., 2011, 2013) and dark spots (Xiao et al., 2013b). Xiao et al. (2013a) noticed that potentially different target material on Mercury might have affected the impact excavation

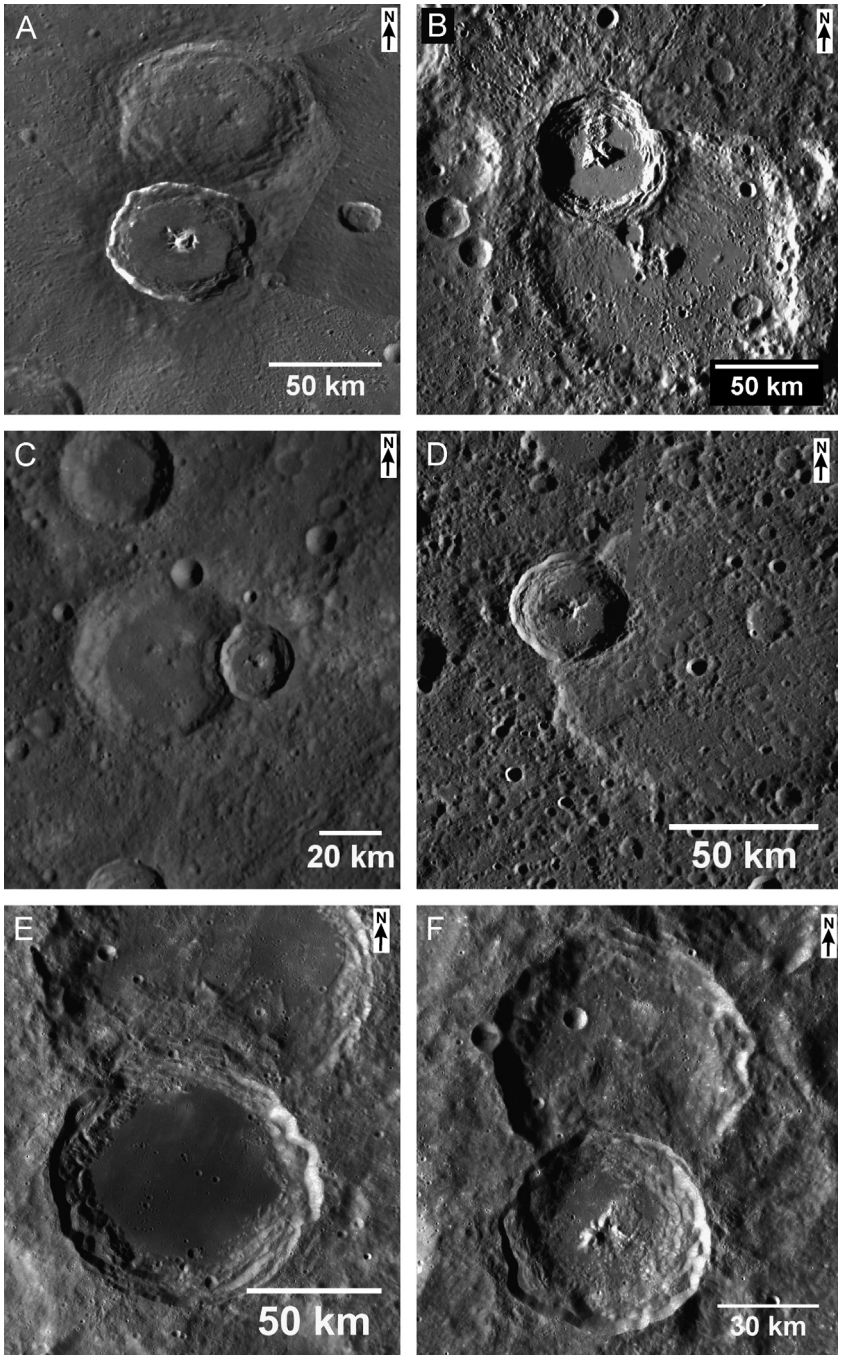

Fig. 8. Most complex craters on Mercury and the Moon do not have ejecta flows, even when they formed on pre-existing slopes. (A) Dégas (D=55 km; 37 °N, 28 °W) on Mercury. (B) Kuiper (D=62 km; 11 °S, 31 °W) on Mercury. (C) An unnamed crater (D=22 km; 9 °N, −125 °E) on Mercury. (D) An unnamed crater (D=41 km; 27 °N, 75 °W) on Mercury. (E) Lomonosov (D=92 km; 27 °N, 98 °E) on the Moon. (F) Moiseev (D=59 km; 10 °N, 103 °E) on the Moon. All figures are in equirectangular projections (250 m/pixel).

process (Melosh, 1989) forming unique crater exterior structures compared with those on the Moon. For instance, secondaries of some craters on Mercury have a more circular morphology than those on the Moon (cf. Xiao et al., 2013a).

With the present image data, the relationship between crustal volatiles on Mercury and the fluidized morphology of the ejecta flows cannot be readily determined. Obvious hollows are visible in some of the parent craters (e.g., Fig. 2C) indicating the pre-impact target surface was richer in volatiles than the average of the planet (Blewett et al., 2013). Crustal volatiles at those locations might have played a role in forming the ejecta flows, and in this case their formation was similar to that of layered ejecta deposits on Mars and Ganymede (e.g., Boyce et al., 2010).

This scenario, however, has several drawbacks:

(1) Stewart et al. (2001) found that SLE form on Mars when ice content at the subsurface is ~10–20% in volume. The content of volatiles in Mercury's crust is as high as that of water ice on Mars and icy satellites.
(2) Craters that have ejecta flows are a common crater population on both Mars and Ganymede (e.g., Barlow, 2010) while only seven such craters are found on Mercury.
(3) Craters having SLE on Mars are usually smaller than 20 km in diameter (e.g., Barlow and Perez, 2003) while those on Mercury are ~30–90 km in diameter (Table 1). Larger martian craters typically display a multiple layer ejecta morphology

due to the effect of crustal volatiles (e.g., Barlow, 2006). We have not found craters with MLEs on Mercury.

(4) Eminescu and Amaral craters on Mercury have relatively circular and isolated secondaries on the facies of secondary clusters and chains (Fig. 1A and C) indicating the pre-impact surface might have different properties (Xiao et al., 2013a). Hollows and dark spots are observed in the crater floors (Fig. 1; Xiao et al., 2013b) suggesting that the pre-impact surfaces may have a high content of sulfide (Blewett et al., 2013; Xiao et al., 2013b). However, neither of the craters exhibits ejecta flows (Fig. 1A and C).

(5) The volatile content in crusts of terrestrial planets is decreasing with time because impact processes keep excavating volatiles from depth and the volatiles are lost upon exposing to space weathering (Kieffer and Simonds, 1980). If there are no additional processes feeding crustal volatiles, the volatile content in Mercury's crust should be higher in the past compared to the present. The observed ejecta flows on Mercury are mostly associated with morphological Class 1–3 craters (Figs. 2 and 3). We should see more ejecta flows around older craters if they have formed due to crustal volatiles.

In summary, we suggest that volatiles might have played a role in forming some of the ejecta flows on Mercury, but no strong observational evidence supports this hypothesis.

4.1.3. *Analog study for the ejecta flows on Mercury and their possible identities*

Layered ejecta structures on planetary surfaces. Image resolution is critical in determining whether these ejecta flows were emplaced in a mode similar to that of some layered ejecta structures, SLE in particular, on other planetary surfaces. The reasons are twofold: (1) SLE reported on Earth, Mars, Ganymede and Europa were considered to have formed during, not after, the impact cratering (e.g., Carr et al., 1977; Barlow and Perez, 2003; Barlow, 2005; Maloof et al., 2010; Boyce et al., 2010). The present image resolution for the seven ejecta flows on Mercury is not sufficiently high enough to determine if they have formed during or after the impact cratering. The ejecta flows could represent a type of mass wasting or avalanche features that postdate their parent craters (see the next section). (2) Terminal ramparts are pronouncedly associated with SLE deposits on both Mars (Garvin et al., 2003) and icy satellites (Boyce et al., 2010). Some SLE deposits do not exhibit obviously raised rims but show thickening towards margins (Wada and Barnouin-Jha, 2006; Komatsu et al., 2007). Potential distal escarpments and thickened deposits might occur at limited sections of the two ejecta flows on Mercury shown in Fig. 2A and B (blue arrows), suggesting that the two ejecta flows might have been emplaced in a similar mode with some SLE deposits on Mars and icy satellites. However, these observations are uncertain due to the limitation in image resolution.

In planar morphology, the ejecta flows on Mercury, especially those with sinuous margins (Fig. 2), are comparable in some ways with layered ejecta structures on Mars. The fluidized appearance and terminal ramparts of typical SLE deposits on Mars (e.g., Fig. 9A) resemble some, but not all, of the mercurian ejecta flows (e.g., blue arrows in Fig. 2A and B). One difference is that layered ejecta structures on Mars usually occur on all sides of their parent craters and no clear local topographic control is visible, whereas the ejecta flows on Mercury are observed only in floors of

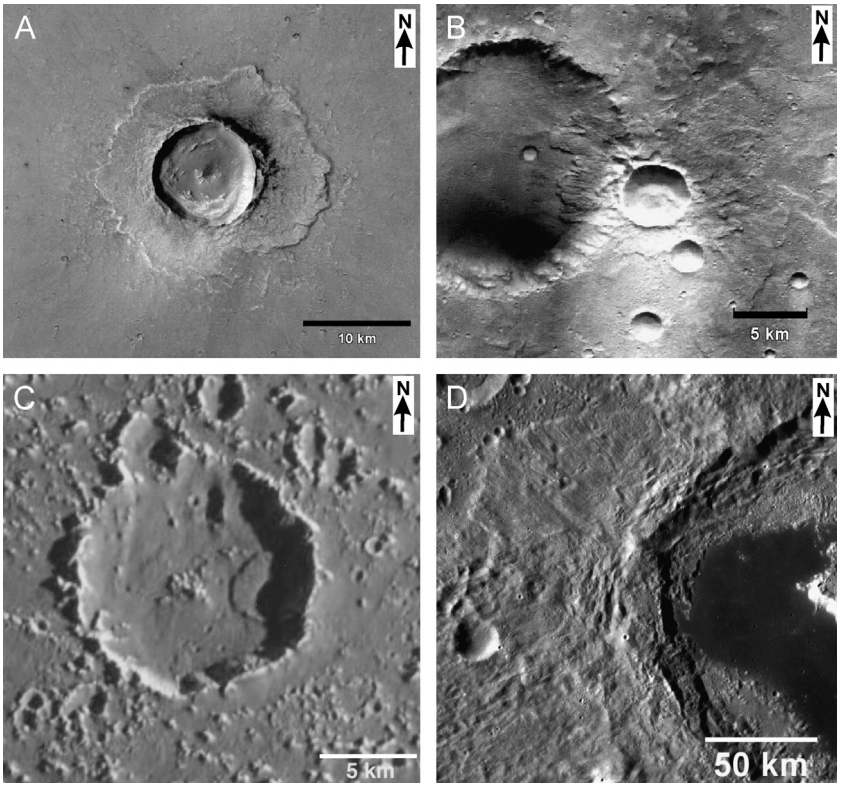

Fig. 9. Some features on other planetary surfaces resemble the ejecta flows on Mercury in the planar morphology. (A) The Belz crater (D=10 km; 21.6 °N, 43.2 °W) on Mars has single layered ejecta deposits. The base image is from the High Resolution Stereo Camera on the Mars Express spacecraft (H5282_0000_ND3, 25 m/pixel, sinusoidal projection). (B) An unnamed crater on Mars (D=5 km; 28.3 °S, 157.2 °E) has single layered ejecta deposits which are most obvious in the floor of the nested crater. The base image is obtained from the High Resolution Stereo Camera (H0228_0000_ND4, 25 m/pixel, sinusoidal projection). (C) A crater on Callisto has a mass wasting deposit in the crater floor that resembles the semicircular ejecta flows on Mercury (110 m/pixel; Greeley et al., 2000). (D) The Tsiolkovsky basin (D=185 km; 21.2 °S, 128.9 °E) on the Moon has ejecta flows on the western ejecta blanket. The base image is from the LROC WAC global mosaics with a resolution of 100 m/pixel.

underlying craters (Figs. 2 and 3). However, Fig. 9B shows an impact crater with a layered ejecta structure on Mars, where the layered morphology is more pronounced in the floor of an older underlying crater (Komatsu et al., 2007). These morphological similarities between the ejecta flows on Mercury and layered ejecta structures on Mars imply some common processes in their formation. The mercurian ejecta flows were probably a result of ejecta fluidization, similar to processes suggested for some martian layered ejecta structures (e.g., Barlow, 1994, 2005; Komatsu et al., 2007). However, factors proposed to be important for martian layered ejecta structures are either absent (atmosphere) or low in quantity (crustal volatiles) in the mercurian environment. This prompts us to explore mechanisms not depending on these factors as discussed later.

Mass wasting deposits. The ejecta flows on Mercury, especially those with semicircular, tapered or tongue-like morphologies (Fig. 3), exhibit some morphological similarities with mass wasting deposits on planetary surfaces (e.g., Fig. 9C). Loose materials on slopes such as crater walls, valleys, and canyons gradually yield to gravity potential until instability occurs in the materials, causing mass movement. Large mass movements associated with impact crater walls, driven by gravity, have various modes of movement such as slides, slumps, flows, and thermal creeping (e.g., Moore et al., 1998). Some mass wasting deposits on planetary surfaces tend to have long runout distances, semicircular or sinuous margins. Radial grooves and lateral sculptures are common features associated with mass wasting deposits, which are not observed with the ejecta flows on Mercury. However, when image resolution is insufficient or the mass wasting deposit is relatively small, these features are not visible. Fig. 9C shows such an example originating from the inner wall of a crater on Callisto (Chuang and Greeley, 2000; Greeley et al., 2000).

Distal ramparts may or may not form with mass wasting deposits because ramparts are related to both the properties of the displaced material and the mode of movement (e.g., Shinbrot et al., 2004; Harrison and Grimm, 2003; Barnouin-Jha et al., 2005). This is consistent with the morphologic characteristics of the ejecta flows on Mercury (Figs. 2 and 3). In general, the ejecta flows on Mercury could be explained as mass wasting deposits, if future high resolution images reveal that they postdated their parent craters.

Ejecta flow of the Tsiolkovsky crater on the Moon. The ejecta flow on the western side of the Tsiolkovsky crater on the Moon (Fig. 9D; $D=180$ km; 20 °S, 129 °E) might have formed as a type of mass wasting feature. It was interpreted as an ejecta avalanche that had emplaced as a dry granular flow (Melosh, 1987). This ejecta flow has no raised rims, occurs at limited sides of the crater and has moved in downslope. It shares similar morphological characteristics with the ejecta flows on Mercury although Tsiolkovsky's ejecta flow is larger in scale.

With the available data in planar morphology, it is plausible that the ejecta flows on Mercury have formed in a way similar to that of the ejecta flow of Tsiolkovsky. The timing of formation is uncertain, but it must have occurred either during or after the impact cratering. Such granular flows generally require the target material to be initially composed of loose, fine grain materials or that the impact itself has produced an enormous amount of fine grain material as part of the excavation process (Schultz, 1992; Boyce and Mouginis-Mark, 2006). The dry granular flow model should operate in nearly any environment on silicate planetary surfaces (Barnouin-Jha et al., 2005; Aranson and Tsimring, 2006; Wada and Barnouin-Jha, 2006). Rampart formation does not necessarily occur with dry granular flow process (Wada and Barnouin-Jha, 2006), a fact consistent with the lack of clear terminal rampart for the mercurian ejecta flows.

Harrison and Grimm (2003) suggested that acoustic fluidization is the most possible driving mechanism for ejecta flows on airless silicate bodies. If this scenario holds, the ejecta flows on Mercury may have formed when an initial instability occurred in the ejecta deposits due to the increasing acoustic field (Melosh, 1979, 1987). When acoustic waves of sufficient strength are transmitted elastically through the individual particles in the ejecta, intraparticle rarefaction waves produce short periods of decreased overburden pressure, temporarily reducing basal resistance and form the ejecta flows (Barnouin-Jha et al., 2005; Harrison and Grimm, 2003).

Another line of evidence potentially supporting the dry granular flow hypothesis for the ejecta flows on Mercury is that more ejecta flows, although still relatively rare compared with those on Mars and Ganymede, are observed on Mercury than on the Moon. Ejecta flows have been reported around several lunar craters, including Tsiolkovsky (Guest and Murray, 1969), Tycho (Shoemaker et al., 1968) and Aristarchus (Guest, 1973). We carefully examined these craters with LROC images and found that the reported ejecta flows of Tycho (Fig. 1D) and Aristarchus are drastically different from that of Tsiolkovsky (Fig. 9D). To date, only the Tsiolkovsky crater on the Moon is confirmed to exhibit an ejecta flow that moved a long distance. Mercury has been more heavily battered than the Moon due to both the larger median impact velocity and impact flux (Cintala, 1992; Le Feuvre and Wieczorek, 2008). Surface material on Mercury should have suffered greater comminution thus are finer. Regardless of other factors, acoustic fluidization occurs more easily in fine particles due to the lower friction between particles and underlying terrains (Boyce et al., 2010; Collins and Melosh, 2003). Therefore, it is plausible that ejecta flows tend to occur more easily on Mercury than on the Moon. The reason that only 7 ejecta flows have been identified on Mercury may be that older ejecta flows might have occurred on Mercury but subsequently been eroded.

In conclusion, the ejecta flows on Mercury probably have formed by fluidization within the ejecta materials. In the context of an airless and relatively low volatile environment of Mercury, the ejecta flows on Mercury are most likely to be dry granular flows that were emplaced during or after the impact cratering process as a type of avalanche deposits, possibly driven by acoustic fluidization.

4.2. Comparison between central pit craters on Mercury and other planetary bodies, and implications for their formation mechanisms

The central pit craters on Mercury are all fresh and several are rayed craters. The large pit sizes relative to the parent crater ($D_p/D_c=\sim$0.09–0.20; Fig. 6) suggest that their formation process should be energetic. The central pits are different from the other forms of depressions on Mercury in the following ways:

(1) Typical secondaries are irregular in shape (Oberbeck and Morrison, 1974). Degraded secondaries are sometimes rimless and circular, which resemble some of the described central pits on Mercury (e.g., Fig. 4). However, some central pits on Mercury are located in rayed craters indicating the pits are unlikely to be degraded secondaries. Distant secondaries formed from impacts of high-velocity ejecta could be circular in shape (McEwen and Bierhaus, 2006; Xiao and Strom, 2012), but the circular or elongated central pits on Mercury are sometimes rimless (e.g., Fig. 4A) and have a cone-shaped morphology (e.g., Fig. 4B), which are different from distant secondaries.
(2) Irregularly-shaped, rimless, and bright-haloed hollows are observed at all longitudes on Mercury (Blewett et al., 2011,

2013). Some hollows without bright halos may represent a final evolutionary stage (Blewett et al., 2013). These hollows can occur on central peaks and are similar to the observed summit pits in morphology. However, hollows usually occur in swarms, and they generally have smaller depths (usually dozens of meters; Blewett et al., 2011; Xiao et al., 2013b) than the central pits. Also, hollows have not been observed in the northern plains material (Blewett et al., 2013; Xiao et al., 2013b), probably because the volatile content in the northern plains is lower than that in intercrater plains (Weider et al., 2012). However, central pit craters are found in the northern plains, indicating the pits are different from hollows.

(3) Volcanic pits on Mercury are usually rimless and irregular in shape, and some can have a size range similar to that of the observed central pits (Kerber et al., 2009, 2011; Gillis-Davis et al., 2009). Volcanic pits can occur on various terrains and sometimes on central peaks of impact craters (Goudge et al., 2012). Documented volcanic pits in fresh impact craters on Mercury usually have reddish (Goudge et al., 2012) or darkish pyroclastic deposits (Xiao et al., 2012). However, the central pits are not associated with color anomalies or volcanic edifices as seen in MDIS images.

Central pits on the Moon are all located on summits of central peaks (Allen, 1975). On Mars, central pits widely occur in both crater floors (i.e., floor pits; Barlow, 2005) and summits of central peaks (i.e., summit pits; Barlow, 2005) (Fig. 10A and B). Central pits on Ganymede and Callisto are all floor pits (Bray et al., 2012). Here we compare the central pits on Mercury and those on other planetary bodies to investigate their possible origins.

4.2.1. Transition from central pit crater to peak-clustered crater

During the impact process, if the target material is too weak to support the rebounding central peak, a floor pit or summit pit may be created by the collapse of the central peak (Passey and Shoemaker, 1982; Melosh and Ivanov, 1999) forming a peak clustered structure. This is the central peak collapse model of forming central pits (Greeley et al., 1982; Passey and Shoemaker, 1982). We argue that the observed central pit craters on Mercury may not represent an intermediate step between central-peak craters and peak-clustered craters. The reasons are twofold: (1) similar-sized craters with a similar age (i.e., same morphological group) in the same region can either have or have no central pits (e.g., Fig. 4C). (2) The transition diameter from complex crater to peak ring crater on Mercury is ~70 km (Baker et al., 2011) which is much larger than the 16–33 km diameter range of the central pit craters (Table 2).

4.2.2. Involvement of crustal volatiles during the impact process

Forming central pit craters on Mars and icy satellites is generally thought to relate to presence of subsurface volatiles (e.g., Barlow, 2010; Senft and Stewart, 2011; Elder et al., 2012). Three different scenarios have been proposed:

(1) The central peak collapse model that involves the influence of subsurface volatiles (Passey and Shoemaker, 1982). Volatiles have smaller strength than silicate rocks therefore the rebounding central peaks collapse more easily.

(2) Croft (1983) suggested that on Mars and icy satellites, if the rebounding peak material contained volatiles, they would drain through fractures within the brecciated interior of the

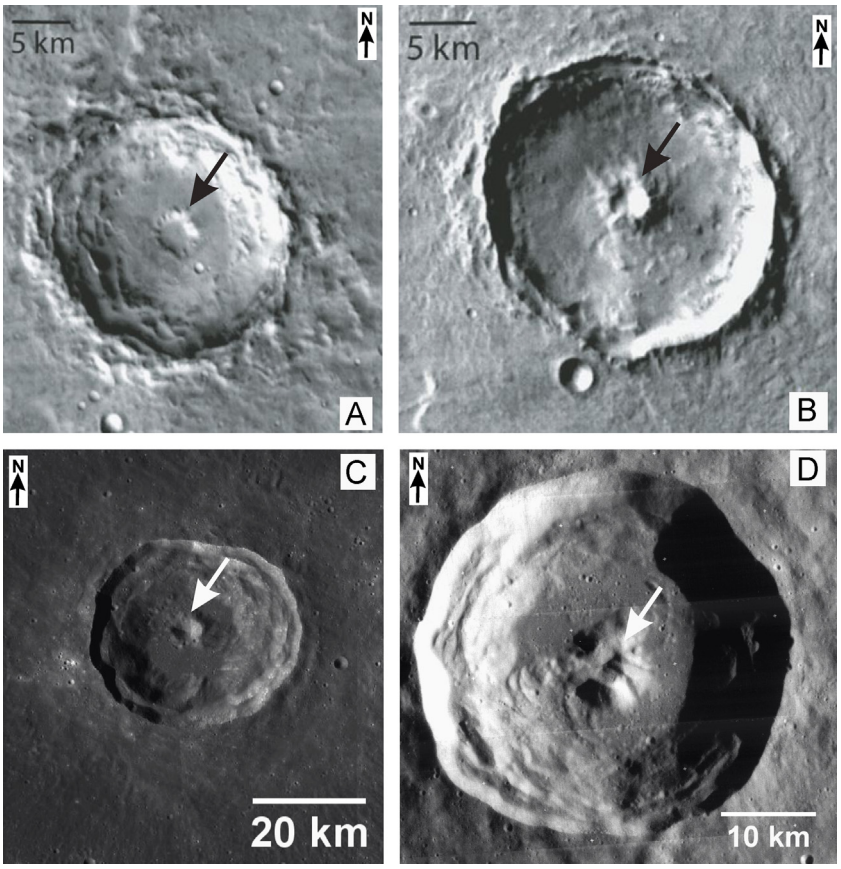

Fig. 10. Central-pit craters on the Moon and Mars. (A) and (B) show a floor pit crater and a summit pit crater on Mars respectively (Barlow, 2010; THEMIS daytime infrared images; 100 m/pixel). (C) and (D) are Timocharis and Lansberg craters on the Moon, respectively. The base mosaic of (C) is from the LROC WAC global mosaics of the Moon (equirectangular projection; 100 m/pixel). The base mosaic of (D) is from Lunar Orbiter IV 4125 (31 m/pixel). (C) and (D) are in equirectangular projections.

crater floor forming central pits. This model has been verified numerically by Elder et al. (2012) and Senft and Stewart (2011). Recent studies favor this model for the origin of floor-pit craters on Mars and Ganymede (Alzate and Barlow, 2011; Bray et al., 2012).

(3) Wood et al. (1978) suggested that central pits form from explosive decompression of near-surface volatiles during crater formation. The region underlying the center of the transient cavity experienced temperatures high enough for volatile vaporization (Barlow, 2010). This model is supported by numerical modeling of impacts in ice soil mixtures and pure ice targets (Pierazzo et al., 2005). However, some central pits on Mars and icy satellites have no rims or the rim deposits have a larger volume than the central pits (Bray et al., 2012) indicating that the volatile-explosion model might not be appropriate to explain their origin. Moreover, impact-produced vapor occurs in the initial excavation stage of an impact event and it is quickly expelled from the excavation cavity, retaining little time to form the pits.

Here we argue that the central pit craters on Mercury do not form due to the effect of crustal volatiles on impact cratering. The reasons are the following:

(1) Alzate and Barlow (2011) and Elder et al. (2012) found that the D_p/D_c of floor-pit craters on Ganymede is larger than that on Mars (Table 4), and they ascribed this difference to the purer ice in Ganymede's crust that formed more melting during impact processes. Mercury has a lower content of crustal volatiles compared with Mars, but the mercurian central pit craters have a comparable median value of D_p/D_c with that of Mars (Table 4).

(2) Central pits on Mercury occur only in fresh Class 1 craters and some have distinct rays. Pit craters on Mars and Ganymede occur in craters with various degradation states (e.g., Barlow, 2010). Older craters should form central pits more easily on Mercury due to the possibly higher content of crustal volatiles in the past.

(3) Seven of the observed central pit craters are located in the northern plains while eight are located in the Caloris exterior plains. Although these plains are both volcanic plains (Strom et al., 2008; Murchie et al., 2008; Head et al., 2011), the volatile content (e.g., sulfur) in the northern plains is lower than that in the Caloris exterior plains (Blewett et al., 2013; Weider et al., 2012). If volatiles have affected the formation of the central pit craters on Mercury, we would see far more central pit craters in the Caloris exterior plains than in the northern plains.

(4) The pre-impact surfaces of complex craters hosting bright haloed hollows have a relatively high volatile content on Mercury (Blewett et al., 2011, 2013). Central pits are not observed in these craters (e.g., Fig. 11; Blewett et al., 2013).

(5) Central pit craters on Mars usually have layered ejecta deposits (Barlow, 2005). The observed central pit craters on Mercury do not have ejecta flows (Figs. 4 and 5), and vice versa (Figs. 2 and 3).

Table 4
Size of central pits and their host craters on planetary bodies.

Planetary body and crater	Diameter range of host craters (D_c, km)	Diameter ratio of central pit and host crater (D_p/D_c)	Median ratio (D_p/D_c)
Mercury (This study, Table 2)	16–33	0.09–0.20	0.12
The Moon (Allen, 1975)[a]	~10–100		
Mars summit pit craters (Barlow, 2010)	5.5–125.4	0.02–0.29	0.12
Mars floor pit craters (Barlow, 2010)	5.0–156.9	0.02–0.48	0.16
Ganymede floor pit craters (Alzate and Barlow, 2011)	~5–150	0.11–0.38	0.19
Callisto floor pit craters (Schenk, 1993)	43–80	0.1–0.45	0.25

[a] Allen (1975) did not report the raw data (diameter, location, etc.) for their observed central-pit craters on the Moon.

These observations contradict the assumption that the central pit craters on Mercury formed due to the effects of target volatiles.

On the other hand, Senft and Stewart (2011) mentioned that cometary impacts on icy satellites could form a gap in the excavation flow and at the same time form a hot plug (target ice that is above the melting line) in the excavation center. Drainage of melted ice in the hot plug could form a floor pit (Senft and Stewart, 2011; Elder et al., 2012). Croft (1983) suggested that some floor-pit craters on Ganymede and Callisto resulted from cometary impacts due to a larger impact velocity causing higher degree of melting. However, volatiles in projectiles (e.g., comets) would be easily vaporized during the contact stage of an impact (Pierazzo and Melosh, 2000) because complete vaporization for ice occurs at shock pressures far smaller than 100 GPa (e.g., Ahrens and O'Keefe, 1985; Stewart et al., 2001). Current understanding about the fate of projectiles during the impact process suggests that vaporized volatiles from projectiles would be rapidly expelled from the excavation cavity during the excavation stage (Pierazzo and Melosh, 2000). However, the central pits on Mercury either occur on crater floors (Figs. 4 and 5) or central peaks indicating the pits formed during or after the excavation stage in impact processes. Therefore, cometary impact is unlikely to be the origin for the central pit craters on Mercury.

4.2.3. *Forming central pit craters without target volatiles*

The Moon and Mercury were once considered to be devoid of central pit craters because their crusts were supposed to have a low content of volatiles (Barlow, 2006; Elder et al., 2012). The observed central pit craters on the Moon (Allen, 1975) and Mercury provide a useful end member to prove that central pits can form without crustal volatiles.

Allen (1975) made the first inventory for central pit craters on the Moon using Lunar Orbiter data. Their catalog did not cover the whole Moon and needs to be updated with present high-quality image data. Allen (1975) argued that the lunar central pits were young volcanoes. Croft (1981) believed that during the crater floor rebounding process in an impact event, a competent outer shell covers more severely brecciated rocks in the center. These two components make an uplift massif forming a central peak. The competent outer shell uplifts more slowly and stops earlier, allowing small amounts of brecciated core material to flow out, forming a void on top of the central peak. The brecciated material is then covered by impact melt in the crater floor. Croft (1983) suggested that the brecciated material in central peaks on the Moon had drained through subsurface fractures forming a depression. Elder et al. (2012) modeled this melt drainage scenario and suggested that on the Moon and Earth, melted silicate rocks will freeze quickly before a large volume is able to drain through subsurface fractures. Bray et al. (2012) also noted that if drainage or outflow of impact melt/breccia could have caused the lunar central pits, central pits should more commonly occur in larger complex craters. So far, the origin of the central pit craters on the Moon remains a puzzle.

The Moon and Mercury have a significantly lower content of crustal volatiles compared with Mars and icy satellites. It is

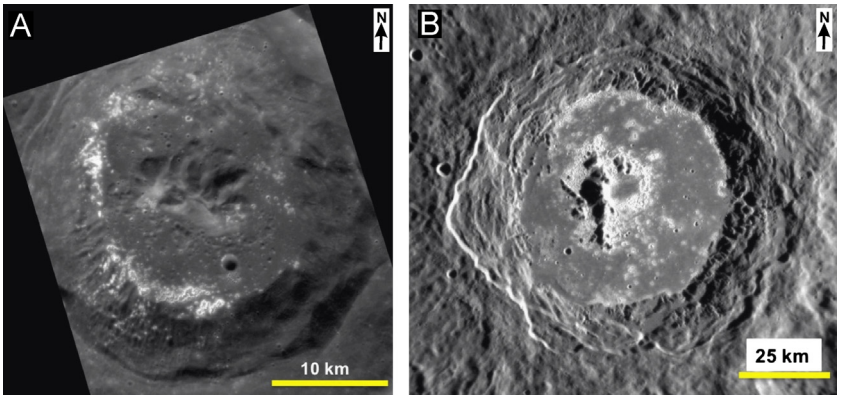

Fig. 11. Many complex craters on Mercury have bright haloed hollows in the crater floors but no central pits are observed. These two images are referred from Blewett et al., 2013). (A) An unnamed crater (D=33 km; 38 °N, −39 °E). The base image is EN0241252210M (26 m/pixel; sinusoidal projection). (B) Warhol crater (D=90 km; 3 °S, −6 °E). The base image is EN0220760132M (128 m/pixel; sinusoidal projection).

possible that the central pit craters on Mercury and the Moon have formed without the involvement of crustal volatiles. Moreover, Mercury's dayside has a higher surface temperature than that on the Moon. When an impact crater forms in Mercury's dayside, the impact melt may stay molten for a longer time and permit a larger portion of melt to drain through subsurface fractures. However, this assumption needs to be tested in future work.

4.2.4. *Effect of impact velocity*

On Mars and Ganymede, similar-sized craters in the same region that have similar degradation states can have or have no central pits (e.g., Barlow and Bradley, 1990; Barlow, 2010). This characteristic is also found on Mercury (e.g., Fig. 4C). Senft and Stewart (2011) found that on icy satellites such as Ganymede, the amount of impact melt was affected by impact velocities for same-sized craters (note: the sizes of the impactors are not necessarily the same). Fundamentally, impact velocity can affect the occurrence of floor pits on Mars (Elder et al., 2012) and icy satellites (Senft and Stewart, 2011) because of the amount of impact produced melt. Abnormally high-velocity impacts produce a large amount of vaporization, abnormally low-velocity impacts produce too little melting (Senft and Stewart, 2011).

Similarly, larger impact velocity forms more melting and greater comminution in silicate targets (Cintala, 1992). If the impact-breccia outflow model (Croft, 1981) or the impact melt/breccia drainage model (Croft, 1983) could explain the origin for the central pit craters on Mercury, the large range of impact velocities (Minton and Malhotra, 2010) on Mercury could explain the observation that same-sized craters in a same region may have or have not central pits on Mercury.

In summary, our current understanding for the central pit craters suggest that they do not need crustal volatiles to form and cometary impact is not a reasonable formation mechanism. They might have formed in a similar manner with central pit craters on the Moon, which deserve further work to unlock.

4.3. *Future work*

Image resolution is critical in analyzing the detailed morphological characteristics for the ejecta flows and central pits on Mercury. For example, high-resolution images will be helpful to reveal if all the central pit craters on Mercury are indeed summit-pit craters. High-quality topographic data (MLA or MDIS stereo data) can accurately measure the geometric parameters for the ejecta flows and central pits. For example, SLE morphologies on Mars (e.g., Garvin et al., 2003) and Ganymede (Boyce et al., 2010) usually have terminal ramparts, but this feature cannot be readily observed for the ejecta flows on Mercury. These limitations restrict our understanding of their possible formation mechanisms. Also, the lithological and physical properties of Mercury's crust are poorly known, especially with respect to the volatile constitution, distribution, and concentration in the crust. These factors are fundamental to understanding the potential effect of target properties on impact processes on Mercury (Xiao et al., 2013a).

5. Conclusions

(1) Craters with ejecta flows and central pits are found with Mercury for the first time. These features occur at all longitudes on the planet and they are morphologically similar with those found on other planetary bodies.
(2) The ejecta flows all move in a downslope direction and they have sinuous or semicircular edges. These features were probably formed by fluidization in the ejecta deposits. The fluidity of the ejecta flows is comparable to those on other planetary bodies. No obvious terminal ramparts, radial striations or secondary craters are visible on the flows in the present image resolution.
(3) Crustal volatiles are not required, although they may help to form the ejecta flows on Mercury. The ejecta flows are most likely to be a type of avalanche features emplaced in form of dry granular flows during or after the impact cratering. Background slope and impact velocity affect their formation.
(4) The central pit craters on Mercury are fresh and several display impact rays. They all occur in smooth plains and intercrater plains. The pits are located on the summits of central peaks when viewing in images with sufficiently high resolution. Some of the pits may occur on crater floors.
(5) Crustal volatiles are not required in forming the central pit craters on Mercury. They likely form in a similar way with the central pit craters on the Moon.

Acknowledgments

We appreciate the constructive comments from Nadine Barlow and an anonymous reviewer, which greatly improved the manuscript. We also appreciate the great help from the guest editor Ken Tanaka in organizing the reviewing processes. Z. Xiao acknowledges the support from Professor Zuoxun Zeng (China University of Geosciences, Wuhan) and Professor Robert G. Strom (Lunar and Planetary Laboratory, University of Arizona) on this project.

References

Ahrens, T.J., O'Keefe, J.D., 1985. Shock vaporization and the accretion of the icy satellites of Jupiter and Saturn. In: Klinger, I., Benest, D., Dollfus, A., Smoluchowski, R. (Eds.), Ices in the Solar System. Kluwer Academic Press, Dordrecht, The Netherlands, pp. 631–654.

Allen, C.C., 1975. Central peaks in lunar craters. The Moon 12, 463–474.

Alvarez, W., Claeys, P., Kieffer, S.W., 1995. Emplacement of Cretaceous-Tertiary boundary shocked quartz from Chicxulub Crater. Science 269, 930–934.

Alzate, N., Barlow, N.G., 2011. Central pit craters on Ganymede. Icarus 211, 1274–1283.

Aranson, I., Tsimring, T., 2006. Patterns and collective behavior in granular media: theoretical concepts. Reviews of Modern Physics 78, 641–687.

Baker, D.M.H., Head, J.W., Prockter, L.M., Schon, S.C., Blewett, D.T., Ernst, C.M., Denevi, B.W., Solomon, S.C., 2011. The transition from complex crater to peak-ring basin on Mercury: new observations from MESSENGER flyby data and constraints on basin formation models. Planetary and Space Science 59 (15), 1932–1948.

Baker, V.R., Komatsu, G., Parker, T.J., Gulick, V.C., Kargel, J.S., Lewis, J.S., 1992. Channels and valleys on Venus: preliminary analysis of Magellan data. Journal of Geophysical Research 97, 13,421–13,444.

Baratoux, D., Delacourt, C., Allemand, P., 2002. An instability mechanism in the formation of the Martian lobate craters and the implications for the rheology of ejecta. Geophysical Research Letters 29 (8), 1210.

Barlow, N.G., 1994. Sinuosity of Martian rampart ejecta deposits. Journal of Geophysical Research 99, 10927–10935, http://dx.doi.org/10.1029/94JE00636.

Barlow, N.G., 2005. A review of Martian impact crater ejecta structures and their implications for target properties. In: Kenkmann, T., Hörz, F., Deutsch, A., (Eds.), Large Meteorite Impacts III, Geological Society of America Special Paper 384, Geological Society of America, Boulder, pp. 433–442.

Barlow, N.G., 2006. Impact craters in the northern hemisphere of Mars: layered ejecta and central pit characteristics. Meteoritics & Planetary Science 41, 1425–1436.

Barlow, N.G., 2010. Central pit craters: observations from Mars and Ganymede and implications for formation models. Geological Society of America Special Papers, vol. 465, pp. 15–27.

Barlow, N.G., Bradley, T.L., 1990. Martian impact craters: correlations of ejecta and interior morphologies with diameter, latitude, and terrain. Icarus 87, 156–179, http://dx.doi.org/10.1016/0019-1035(90)90026-6.

Barlow, N.G., Perez, C.B., 2003. Martian impact crater ejecta morphologies as indicators of the distribution of subsurface volatiles. Journal of Geophysical Research 108 (E8), 5085, http://dx.doi.org/10.1029/2002JE002036.

Barlow, N.G., Boyce, J.M., Costard, F.M., Craddock, R.A., Garvin, J.B., Sakimoto, S.E.H., Kuzmin, R.O., Roddy, D.J., Soderblom, L.A., 2000. Standardizing the nomenclature of Martian impact crater ejecta morphologies. Journal of Geophysical Research 105 (26), 733–826 738.

Barnouin-Jha, O.S., Baloga, S., Glaze, L., 2005. Comparing landslides to fluidized crater ejecta on Mars. Journal of Geophysical Research 110, http://dx.doi.org/10.1029/2003JE002214.

Blewett, D.T., Chabot, N.L., Denevi, B.W., Ernst, C.M., Head, J.W., Izenberg, N.R., Murchie, S.L., Solomon, S.C., Nittler, L.R., McCoy, T.J., Xiao, Z., Baker, D.M.H., Fassett, C.I., Braden, S.E., Oberst, J., Scholten, F., Preusker, F., Hurwitz, D.M., 2011. Hollows on Mercury: MESSENGER evidence for geologically recent volatile-related activity. Science 333, 1856–1859.

Blewett, D.T., Vaughan, W.M., Xiao, Z., Chabot, C.L., Denevi, B.W., Ernst, C.M., Helbert, J., D'Amore, M., Maturilli, A., Head, J.W., Solomon, S.C., 2013 Mercury's hollows: constraints on formation and composition from analysis of geological setting and spectral reflectance. Journal of Geophysical Research 118, 1–20, http://dx.doi.org/10.1029/2012JE004174.

Boyce, J., Barlow, N., Mougins-Mar, P., Stewart, S., 2010. Rampart craters on Ganymede: their implications for fluidized ejecta emplacement. Meteoritics & Planetary Science 45 (4), 638–661.

Boyce, J.M., Mouginis-Mark, P.J., 2006. Martian craters viewed by the THEMIS instrument: double-layered craters. Journal of Geophysical Research 111 (E10), http://dx.doi.org/10.1029/2005JE2638.

Bray, V.J., Tornabene, L.L., Keszthelyi, L., McEwen, A .S., Hawke, B.R., Giguere, T., Kattenhorn, S., Garry, W., Rizk, B., Caudill, C., Gaddis, L.R., van der Bogert, C., 2010. New insight into lunar impact melt mobility from the LRO Camera. Geophysical Research Letters 37 (L21202), 1-5, http://dx.doi.org/10.1029/2010GL044666.

Bray, V.J., Schenk, P.M., Melosh, H.J., Morgan, J.V., Collins, G.S., 2012. Ganymede crater dimensions—implications for central peak and central pit formation and development. Icarus 217, 115–129.

Carr, M.H., Crumpler, L.S., Cutts, J.A., Greeley, R., Guest, J.E., Masursky, H., 1977. Martian impact craters and the emplacement of ejecta by surface flow. Journal of Geophysical Research 82, 4055–4065.

Cavanaugh, J.F., Smith, J.C., Sun, X., Bartels, A.E., Ramos-Izquierdo, L., Krebs, D.J., McGarry, J.F., Trunzo, R., Novo-Gradac, A.M., Britt, J.L., 2007. The Mercury Laser Altimeter instrument for the MESSENGER mission. Space Science Reviews 131, 451–479, http://dx.doi.org/10.1007/s11214-007-9273-4.

Chuang, F.C., Greeley, R., 2000. Large mass movements on Callisto. Journal of Geophysical Research 105 (E8), 20,227–20,244.

Cintala, M.J., 1992. Impact-induced thermal effects in the lunar and Mercurian regoliths. Journal of Geophysical Research 97, 947–974, http://dx.doi.org/10.1029/91JE02207.

Collins, G.S., Melosh, H.J., 2003. Acoustic fluidization and the extraordinary mobility of sturztstroms. Journal of Geophysical Research 108 (B10), 2473, http://dx.doi.org/10.1029/2003JB002465.

Croft, S.M., 1981. On the origin of pit craters. Lunar and Planetary Science XII, 196–198.

Croft, S.M., 1983. A proposed origin for palimpsests and anomalous pit craters on Ganymede and Callisto. In: Proceedings of the Lunar Science Conference, vol. 14; Journal of Geophysical Research, vol. 88, pp. B71–B89.

Denevi, B.W., Robinson, M.S., Solomon, S.C., Murchie, S.L., Blewett, D.T., Domingue, D.L., McCoy, T.J., Ernst, C.M., Head, J.W., Watters, T.R., Chabot, N.L., 2009. The evolution of Mercury's crust: a global perspective from MESSENGER. Science 324, 613–619.

Denevi, B.W., Robinson, M.S., Murchie, S.L., Ernst, C.M., Byrne, P.K., Solomon, S.C., Peplowski, P.N., 2012. The distribution of young plains on Mercury. EPSC Abstracts and Program 7, abstract EPSC2012-812.

Elder, C.M., Bray, V.J., Melosh, H.J., 2012. The theoretical plausibility of central pit crater formation via melt drainage. Icarus 221, 831–843.

Garner, K.M.L., Barlow, N.G., 2012. Distribution of rimmed, partially rimmed, and non-rimmed central floor pits on Mars. In: Proceedings of 43rd Lunar and Planetary Science Conference, Abstract #1256.

Garvin, J.B., Sakimoto, S.E.H., Frawley, J.J., 2003. Craters on Mars: global geometric properties from gridded MOLA topography. In: Proceedings of 6th International Conference on Mars, Houston, Texas, Lunar and Planetary Institute, Abstract no. 3277.

Gillis-Davis, J.J., Blewett, D.T., Gaskill, R.W., Denevi, B.W., Robinson, M.S., Strom, R.G., Solomon, S.C., Sprague, A.L., 2009. Pit-floor craters on Mercury: evidence of near-surface igneous activity. Earth Planet Science Letter 285, 243–250.

Goudge, T.A., Head, J.W., Kerber, L., Blewett, D.T., Denevi, B.W., Murchie, S.L., Izenberg, N.R., McClintock, W.E., Holsclaw, G.M., Domingue, D.L., Gillis-Davis, J.J., Xiao, Z., Strom, R.G., Helbert, J., Solomon, S.C, 2012. Global inventory and characterization of pyroclastic deposits on Mercury: new insights into pyroclastic activity from MESSENGER orbital data. 43rd Lunar and Planetary Science Conference, Abstract 1325.

Greeley, R., Fink, J.H., Gault, D.E., Guest, J.E., 1982. Experimental simulation of impact cratering on icy satellites. In: Morrison, D. (Ed.), 1982. Satellites of Jupiter, pp. 340–378.

Greeley, R., Klemaszewski, J.E., Wagner, R., the Galileo Imaging Team, 2000. Galileo views of the geology of Callisto. Planetary and Space Science 48, 829–853.

Guest, J.E., 1973. Stratigraphy of ejecta from the lunar crater Aristarchus. Geological Society of America Bulletin 84, 2873–2893.

Guest, J.E., Murray, J.B., 1969. Nature and origin of Tsiolkovsky Crater, lunar farside. Planetary and Space Science 17, 121–141.

Hack, J.T., 1960. Interpretation of erosional topography in humid temperate regions. American Journal of Science 258-A, 80–97.

Harrison, K.P., Grimm, R.E., 2003. Rheological constraints on Martian landslides. Icarus 163, 347–362.

Hawkins, S.E., Boldt, J.D., Darlington, E.H., Espiritu, R., Gold, R.E., Gotwols, B., Grey, M.P., Hash, C.D., Hayes, J.R., Jaskulek, S.E., Kardian Jr., C.J., Keller, M.R., Malaret, E. R., Murchie, S.C., Murphy, P.K., Peacock, K., Prockter, L.M., Reiter, R.A., Robinson, M.S., Schaefer, E.D., Shelton, R.G., Sterner II, R.E., Taylor, H.W., Watters, T.R., Williams, B.D., 2007. The Mercury Dual Imaging System on the MESSENGER Spacecraft. Space Science Reviews 131, 247–338.

Head III, J.W., Chapman, C.R., Strom, R.G., Fassett, C.I., Denevi, B.W., Blewett, D.T., Ernst, C.M., Watters, T.R., Solomon, S.C., Murchie, S.L., Prockter, L.M., Chabot, N.L., Gillis-Davis, J.J., Whitten, J.L., Goudge, T.A., Baker, D.M.H., Hurwitz, D.M., Ostrach, L.R., Xiao, Z., Merline, W.J., Kerber, L., Dickson, J.L., Oberst, J., Byrne, P.K., Klimczak, C., Nittler, L.R., 2011. Flood volcanism in the northern high latitudes of Mercury revealed by MESSENGER. Science 333, 1853–1856, http://dx.doi.org/10.1126/science.1211997.

Kargel, J.S., 1989. First and second-order equatorial symmetry of Martian rampart crater ejecta morphologies. In: Proceedings of Fourth International Conference on Mars, Tucson, University of Arizona, pp. 132–133.

Kenkmann, T., Schönian, F., 2006. Ries and Chicxulub: impact craters on Earth provide insights for Martian ejecta blankets. Meteoritics and Planetary Science 41, 1587–1603, http://dx.doi.org/10.1111/j.1945-5100.2006.tb00437.x.

Kerber, L., Head, J.W., Solomon, S.C., Murchie, S.L., Blewett, D.T., Wilson, L., 2009. Explosive volcanic eruptions on Mercury: eruption conditions, magma volatile content, and implications for interior volatile abundances. Earth and Planetary Science Letters 285, 263–271.

Kerber, L., Head, J.W., Blewett, D.T., Solomon, S.C., Wilson, L., Murchie, S.L., Robinson, M.S., Denevi, B.W., Domingue, D.L., 2011. The global distribution of pyroclastic deposits on Mercury: the view from MESSENGER flybys 1–3. Planetary and Space Science 59, 1895–1909.

Kieffer, S.W, Simonds, C.H., 1980. The role of volatiles and lithology in the impact cratering process. Reviews of Geophysics and Space Physics 18, 143–181.

Komatsu, G., Ori, G.G., Di Lorenzo, S., Rossi, A.P., Neukum, G., 2007. Combinations of processes responsible for Martian impact crater "layered ejecta structures" emplacement. Journal of Geophysical Research 112, E06005, http://dx.doi.org/10.1029/2006JE002787.

Le Feuvre, M.L., Wieczorek, M.A., 2008. Nonuniform cratering of the terrestrial planets. Icarus 197, 291–306, http://dx.doi.org/10.1016/j.icarus.2008.04.011.

Lewis, J.S., 1972. Metal/silicate fractionation in the Solar System. Earth and Planetary Science Letters 15, 286–290.

Maloof, A.C., Stewart, S.T., Weiss, B.P., Soule, S.A., Swanson-Hysell, N.L., Louzada, K.L., Garrick-Bethell, I., Poussart, P.M., 2010. Geology of Lonar Crater, India. Geological Society of America Bulletin 122, 109–126.

McEwen, A.S., Bierhaus, E.B., 2006. The importance of secondary cratering to age constraints on planetary surfaces. Annual Review of Earth and Planetary Sciences 34, 540–567.
McGetchin, T.R., Settle, M., Head, J.W., 1973. Radial thickness variation in impact crater ejecta: implications for lunar basin deposits. Earth and Planetary Science Letters 20, 226–236.
Melosh, H.J., 1979. Acoustic fluidization: a new geologic process? Journal of Geophysical Research 84, 7513–7520.
Melosh, H.J., 1987. The mechanics of large rock avalanches, Debris Flows/Avalanches: Process, Recognition, and Mitigation. Reviews in Engineering Geology, vol. 7, J.E. Costa, J.E., Wieczorek, G.F., (Eds.), Geological Society of America, Boulder, Colorado, pp. 1–12.
Melosh, H.J., 1989. Impact Cratering. Oxford University Press, New York 245 pp.
Melosh, H.J., Ivanov, B.A., 1999. Impact crater collapse. Annual Review of Earth and Planetary Sciences 27, 385–415, http://dx.doi.org/10.1146/annurev.earth.27.1.385.
Milton, D.J., Barlow, B.C., Brett, R., Brown, A.R., Glikson, A.Y., Manwaring, E.A., Moss, F.J., Sedmik, E.C.E., van Son, J., Young, G.A., 1972. Gosses bluff impact structure, Australia. Science 175 (4027), 1199–1207.
Minton, D.A., Malhotra, R., 2010. Dynamical erosion of the asteroid belt and implications for large impacts in the inner Solar System. Icarus 207, 744–757, http://dx.doi.org/10.1016/j.icarus.2009.12.008.
Moore, J.M., Asphaug, E., Sullivan, R.J., Klemaszewski, J.E., Bender, K.C., Greeley, R., Geissler, P.E., McEwen, A.S., Turtle, E.P., Phillips, C.B., Tufts, B.R., Head III, J.W., Pappalardo, R.T., Jones, K.B., Chapman, C.R., Belton, M.J.S., Kirk, R.L., Morrison, D., 1998. Large impact features on Europa: results of the Galileo nominal mission. Icarus 135, 127–145.
Moore, J.M., Asphaug, E., Belton, M.J.S., Bierhaus, B., Breneman, H.H., Brooks, S.M., Chapman, C.R., Chuang, F.C., Collins, G.C., Giese, B., Greeley, R., Head, J.W., Kadel, S., Klaasen, K.P., Klemaszewski, J.E., Magee, K.P., Moreau, J., Morrison, D., Neukum, G., Pappalardo, R.T., Phillips, C.B., Schenk, P.M., Senske, D.A., Sullivan, R.J., Turtle, E.P., Williams, K.K., 2001. Impact features on Europa: results of the Galileo Europa Mission (GEM). Icarus 151, 93–111, http://dx.doi.org/10.1006/icar.2000.6558.
Mouginis-Mark, P.J., 1978. Morphology of Martian rampart craters. Nature 272, 870–872.
Mouginis-Mark, P.J., 1979. Martian fluidized ejecta morphology: variations with crater size, latitude, altitude, and target material. Journal of Geophysical Research 84, 8011–8022.
Murchie, S.L., Watters, T.R., Robinson, M.S., Head, J.W., Strom, R.G., Chapman, C.R., Solomon, S.C., McClintock, W.E., Prockter, L.M., Domingue, D.L., Blewett, D.T., 2008. Geology of the Caloris basin, Mercury: a view from MESSENGER. Science, 321; , pp. 73–76.
Nittler, L.R., Starr, R.D., Weider, S.Z., McCoy, T.J., Boynton, W.V., Ebel, D.S., Ernst, C.M., Evans, L.G., Goldsten, J.O., Hamara, D.K., Lawrence, D.J., McNutt Jr., R.L., Schlemm II, C. E., Solomon, S.C., Sprague, A.L., 2011. The major-element composition of Mercury's surface from MESSENGER X-ray spectrometry. Science 333, 1847–1850.
O'Keefe, J.D., Stewart, S.T., Lainhart, M.E., Ahrens, T.J., 2001. Damage and rock–volatile mixture effects on Impact Crater formation. International Journal of Impact Engineering 26, 543–553.
Oberbeck, V.R., Morrison, R.H., 1974. Laboratory simulation of the herringbone pattern associated with lunar secondary crater chains. Moon 9, 415–455, http://dx.doi.org/10.1007/BF00562581.
Osinski, G.R., 2004. Impact melt rocks from the Ries structure, Germany: an origin as impact melts flows? Earth and Planetary Science Letters 226, 529–543.
Osinski, G.R., Tornabene, L.L., Grieve, R.A.F., 2011. Impact ejecta emplacement on terrestrial planets. Earth and Planetary Science Letters 310, 167–181.
Passey, Q.R., Shoemaker, E.M., 1982. Craters and basins on Ganymede and Callisto: morphological indicators of crustal evolution. In: Morrison, D. (Ed.), Satellites of Jupiter. University of Arizona Press, Tucson, pp. 379–434.
Peplowski, R.N., Evans, L.G., Hauck II, S.A., McCoy, T.J., Boynton, W.V., Gillis-Davis, J.J., Ebel, D.S., Goldsten, J.O., Hamara, D.K., Lawrence, D.J., McNutt Jr., R.L., Nittler, L.R., Solomon, S.C., Rhodes, E.A., Sprague, A.L., Starr, R.D., Stockstill-Cahill, K.R., 2011. Radioactive elements on Mercury's surface from MESSENGER: implications for the planet's formation and evolution. Science 333, 1850–1852.
Pierazzo, E., Melosh, H.J., 2000. Hydrocode modeling of oblique impacts: the fate of the projectile. Meteoritics & Planetary Science 35, 117–130.
Pierazzo, E., Artemieva, N.A., Ivanov, B.A., 2005. Starting conditions for hydrothermal systems underneath martian craters: Hydrocode modeling. In: Kenkmann, T., Hörz, F., Deutsch, A., (Eds.), Large Meteorite Impacts III, Geological Society of America Special Paper 384, pp. 443–457.
Ritter, D.F., Kochel, C.R., Miller, J.R., 2006. In: Forth (Ed.), Process Geomorphology. Waveland Press, Long Grove, pp. 79–133.
Robbins, S.J., Hynek, B.M., 2012. A new global database of Mars impact craters≥1 km: 2. Global crater properties and regional variations of the simple-to-complex transition diameter. Journal of Geophysical Research 117, E06001, http://dx.doi.org/10.1029/2011JE003967.
Robinson, M.S., Brylow, S.M., Tschimmel, M., Humm, D., Lawrence, S.J., Thomas, P.C., Denevi, B.W., Bowman-Cisneros, E., Zerr, J., Ravine, M.A., Caplinger, M.A., Ghaemi, F.T., Schaffner, J.A., Malin, M.C., Mahanti, P., Bartels, A., Anderson, J., Tran, T.N., Eliason, E.M., McEwen, A.S., Turtle, E., Jolliff, B.L., Hiesinger, H., 2010. Lunar Reconnaissance Orbiter Camera (LROC) instrument overview. Space Science Review 150 (1–4), 81–124.
Schenk, P.M., 1993. Central pit and dome craters: exposing the interiors of Ganymede and Callisto. Journal of Geophysical Research 98, 7475–7498.
Schultz, P.H., 1992. Ejecta emplacement and crater formation on Venus. Journal of Geophysical Research 97, 16,183–16,248.
Schultz, P.H., Singer, J., 1980. A comparison of secondary craters on the Moon, Mercury and Mars. In: Proceedings of the 11th Lunar Planetary Science Conference, pp. 2243–2259.
Senft, L.E., Stewart, S.T., 2011. Modeling the morphological diversity of impact craters on icy satellites. Icarus 214, 67–81.
Shinbrot, T., Duong, N., Kwan, L., Alvarez, M., 2004. Dry granular flows can generate surface features resembling those seen in Martian gullies. Proceedings of the National Academy of Science 101, 8542–8546.
Shoemaker, E.M., 1965. Preliminary Analysis of the fine Structure of the Lunar surface in Mare Cognitum. In: Ranger 7, Part 2, Experimenters' Analyses and Interpretations. JPL/NASA, pp. 75–134, Technical Report 32-700.
Shoemaker, E.M., Batson, R.M., Holt, H.E., Morris, E.C., Remilson, J.J., Whitaker, E.A., 1968. Television observations from Surveyor VII. Surveyor VII: A Preliminary Report. NASA Special Publications SP-173, 13–81.
Shreve, R.L., 1968. The Blackhawk landslide. Geological Society of America Special Paper, vol. 108, p. 47.
Snyder, D., Tait, S., 1998. A flow-front instability in viscous gravity current. Journal of Fluid Mechanics 369, 1–21.
Solomon, S.C., McNutt Jr., R.L., Gold, R.E., Acuna, M.H., Baker, D.N., Boynton, W.V., Chapman, C.R., Cheng, A.F., Gloeckler, G., Head III, J.W., Krimigis, S.M., McClintock, W.E., Murchie, S.L., Peale, S.J., Phillips, R.J., Robinson, M.S., Slavin, J.A., Smith, D.E., Strom, R.G., Trombka, J.I., Zuber, M.T., 2001. The MESSENGER mission to Mercury: scientific objectives and implementation. Planetary and Space Science 49, 1445–1465.
Stewart, S.T., O'Keefe, J., Ahrens, T., 2001. The relation between rampart crater morphologies and the amount of subsurface ice. In: Proceedings of 32nd Lunar and Planetary Science Conference, p. 2092.
Strom, R.G., 1979. Mercury: a post Mariner-10 assessment. Space Science Reviews 24, 3–70.
Strom, R.G., Chapman, C.R., Merline, W.J., Solomon, S.C., Head, J.W., 2008. Mercury cratering record viewed from MESSENGER's first flyby. Science 321, 79–81, http://dx.doi.org/10.1126/science.1159317.
Wada, K., Barnouin-Jha, O.S., 2006. The formation of fluidized ejecta on Mars by granular flow. Meteoritics & Planetary Science 41, 1551–1569.
Weider, S.Z., Nittler, L.R., Starr, R.D., McCoy, T.J., Stockstill-Cahill, K.R., Byrne, P.K., Denevi, B.W., Head, J.W., Solomon, S.C., 2012. Chemical heterogeneity on Mercury's surface revealed by the MESSENGER X-Ray Spectrometer. Journal of Geophysical Research 117, E00L05, http://dx.doi.org/10.1029/2012JE004153.
Wohletz, K.H., Sheridan, M.F., 1983. Martian rampart crater ejecta: experiments and analysis of melt water interaction. Icarus 56, 15–37.
Wood, C.A., Anderson, L., 1978. New morphometric data for fresh lunar craters. In: Proceedings of the 9th Lunar Planetary Science Conference, pp. 3669–3689.
Wood, C.A., Head, J.W., Cintala, M.J., 1978. Interior morphology of fresh Martian craters: the effects of target characteristics. In: Merrill, R.B. (Ed.), Proceedings of the 9th Lunar and Planetary Science Conference, Houston, New York, Pergamon Press, pp. 3691–3709.
Xiao, Z., Strom, R.G., 2012. Problems determining relative and absolute ages using the small crater population. Icarus 220, 254–267.
Xiao, Z., Strom, R.G., Blewett, D.T., Chapman, C.R., Denevi, B.W., Head, J. W., Fassett, C.I., Braden, S.E., Gwinner, K., Solomon, S.C., Murchie, S.L., Watters, T.R., Banks, M.E., 2012. The Youngest Geologic Terrains on Mercury. In: Proceedings of 43rd Lunar and Planetary Science Conference, p. 2143.
Xiao, Z., Strom, R.G., Chapman, C.R., Head, J.W., Klimczak, C., Ostrach, L.R., Helbert, J., D'Incecco, P., 2013a. Comparisons of fresh complex impact craters on Mercury and the Moon: implications of controlling factors in impact excavation processes. Icarus, http://dx.doi.org/10.1016/j.icarus.2013.10.002.
Xiao, Z., Strom, R.G., Blewett, D.T., Domingue, D.L., Murchie, S.L., Sprague, A.L., Byrne, P.K., Becker, K.J., Solomon, S.C., Helbert, J., 2013b. Dark spots on Mercury: a hollow-related low-reflectance material. Journal of Geophysical Research 118, 1752–1765, http://dx.doi.org/10.1002/jgre.20115.
Zuber, M.T., Smith, D.E., Phillips, R.J., Solomon, S.C., Neumann, G.A., Hauck, S.A., Peale, S.J., Barnouin, O.S., Head, J.W., Johnson, C.L., Lemoine, F.G., Mazarico, E., Sun, X., Torrence, M.H., Freed, A.M., Klimczak, C., Margot, J., Oberst, J., Perry, M.E., McNutt, R.L., Balcerski, J.A., Michel, N., Talpe, M.J., Yang, D., 2012. Topography of the Northern Hemisphere of Mercury from MESSENGER Laser Altimetry. Science 336, 217–220.